Planck 2015 results

Planck 2015 results

VIII. High Frequency Instrument data processing: Calibration and maps

Planck Collaboration: R. Adam[72], P. A. R. Ade[83], N. Aghanim[55], M. Arnaud[70], M. Ashdown[65,5], J. Aumont[55], C. Baccigalupi[82], A. J. Banday[91,9], R. B. Barreiro[60], N. Bartolo[28,61], E. Battaner[92,93], K. Benabed[56,90], A. Benoît[53], A. Benoit-Lévy[22,56,90], J.-P. Bernard[91,9], M. Bersanelli[31,45], B. Bertincourt[55], P. Bielewicz[79,9,82], J. J. Bock[62,11], L. Bonavera[60], J. R. Bond[8], J. Borrill[13,86], F. R. Bouchet[56,85], F. Boulanger[55], M. Bucher[1], C. Burigana[44,29,46], E. Calabrese[88], J.-F. Cardoso[71,1,56], A. Catalano[72,68], A. Challinor[58,65,12], A. Chamballu[70,14,55], H. C. Chiang[25,6], P. R. Christensen[80,33], D. L. Clements[51], S. Colombi[56,90], L. P. L. Colombo[21,62], C. Combet[72], F. Couchot[67], A. Coulais[68], B. P. Crill[62,11], A. Curto[60,5,65], F. Cuttaia[44], L. Danese[82], R. D. Davies[63], R. J. Davis[63], P. de Bernardis[30], A. de Rosa[44], G. de Zotti[41,82], J. Delabrouille[1], J.-M. Delouis[56,90], F.-X. Désert[49], J. M. Diego[60], H. Dole[55,54], S. Donzelli[45], O. Doré[62,11], M. Douspis[55], A. Ducout[56,51], X. Dupac[35], G. Efstathiou[58], F. Elsner[22,56,90], T. A. Enßlin[76], H. K. Eriksen[59], E. Falgarone[68], J. Fergusson[12], F. Finelli[44,46], O. Forni[91,9], M. Frailis[43], A. A. Fraisse[25], E. Franceschi[44], A. Frejsel[80], S. Galeotta[43], S. Galli[64], K. Ganga[1], T. Ghosh[55], M. Giard[91,9], Y. Giraud-Héraud[1], E. Gjerløw[59], J. González-Nuevo[17,60], K. M. Górski[62,94], S. Gratton[65,58], A. Gruppuso[44], J. E. Gudmundsson[25], F. K. Hansen[59], D. Hanson[77,62,8], D. L. Harrison[58,65], S. Henrot-Versillé[67], D. Herranz[60], S. R. Hildebrandt[62,11], E. Hivon[56,90], M. Hobson[5], W. A. Holmes[62], A. Hornstrup[15], W. Hovest[76], K. M. Huffenberger[23], G. Hurier[55], A. H. Jaffe[51], T. R. Jaffe[91,9], W. C. Jones[25], M. Juvela[24], E. Keihänen[24], R. Keskitalo[13], T. S. Kisner[74], R. Kneissl[34,7], J. Knoche[76], M. Kunz[16,55,2], H. Kurki-Suonio[24,40], G. Lagache[4,55], J.-M. Lamarre[68], A. Lasenby[5,65], M. Lattanzi[29], C. R. Lawrence[62], M. Le Jeune[1], J. P. Leahy[63], E. Lellouch[69], R. Leonardi[35], J. Lesgourgues[57,89], F. Levrier[68], M. Liguori[28,61], P. B. Lilje[59], M. Linden-Vørnle[15], M. López-Caniego[35,60], P. M. Lubin[26], J. F. Macías-Pérez[72], G. Maggio[43], D. Maino[31,45], N. Mandolesi[44,29], A. Mangilli[55,67], M. Maris[43], P. G. Martin[8], E. Martínez-González[60], S. Masi[30], S. Matarrese[28,61,38], P. McGehee[52], A. Melchiorri[30,47], L. Mendes[35], A. Mennella[31,45], M. Migliaccio[58,65], S. Mitra[50,62], M.-A. Miville-Deschênes[55,8], A. Moneti[56], L. Montier[91,9], G. Morgante[44], D. Mortlock[51], A. Moss[84], S. Mottet[56], D. Munshi[83], J. A. Murphy[78], P. Naselsky[80,33], F. Nati[25], P. Natoli[29,3,44], C. B. Netterfield[18], H. U. Nørgaard-Nielsen[15], F. Noviello[63], D. Novikov[75], I. Novikov[80,75], C. A. Oxborrow[15], F. Paci[82], L. Pagano[30,47], F. Pajot[55], D. Paoletti[44,46], F. Pasian[43], G. Patanchon[1], T. J. Pearson[11,52], O. Perdereau[67,*], L. Perotto[72], F. Perrotta[82], V. Pettorino[39], F. Piacentini[30], M. Piat[1], E. Pierpaoli[21], D. Pietrobon[62], S. Plaszczynski[67], E. Pointecouteau[91,9], G. Polenta[3,42], G. W. Pratt[70], G. Prézeau[11,62], S. Prunet[56,90], J.-L. Puget[55], J. P. Rachen[19,76], M. Reinecke[76], M. Remazeilles[63,55,1], C. Renault[72], A. Renzi[32,48], I. Ristorcelli[91,9], G. Rocha[62,11], C. Rosset[1], M. Rossetti[31,45], G. Roudier[1,68,62], B. Rusholme[52], M. Sandri[44], D. Santos[72], A. Sauvé[91,9], M. Savelainen[24,40], G. Savini[81], D. Scott[20], M. D. Seiffert[62,11], E. P. S. Shellard[12], L. D. Spencer[83], V. Stolyarov[5,87,66], R. Stompor[1], R. Sudiwala[83], D. Sutton[58,65], A.-S. Suur-Uski[24,40], J.-F. Sygnet[56], J. A. Tauber[36], L. Terenzi[37,44], L. Toffolatti[17,60,44], M. Tomasi[31,45], M. Tristram[67,*], M. Tucci[16], J. Tuovinen[10], L. Valenziano[44], J. Valiviita[24,40], B. Van Tent[73], L. Vibert[55], P. Vielva[60], F. Villa[44], L. A. Wade[62], B. D. Wandelt[56,90,27], R. Watson[63], I. K. Wehus[62], D. Yvon[14], A. Zacchei[43], and A. Zonca[26]

(Affiliations can be found after the references)

ABSTRACT

This paper describes the processing applied to the cleaned, time-ordered information obtained from the *Planck* High Frequency Instrument (HFI) with the aim of producing photometrically calibrated maps in temperature and (for the first time) in polarization. The data from the entire 2.5-year HFI mission include almost five full-sky surveys. HFI observes the sky over a broad range of frequencies, from 100 to 857 GHz. To obtain the best accuracy on the calibration over such a large range, two different photometric calibration schemes have been used. The 545 and 857 GHz data are calibrated using models of planetary atmospheric emission. The lower frequencies (from 100 to 353 GHz) are calibrated using the time-variable cosmological microwave background dipole, which we call the orbital dipole. This source of calibration only depends on the satellite velocity with respect to the solar system. Using a CMB temperature of $T_{CMB} = 2.7255 \pm 0.0006$ K, it permits an independent measurement of the amplitude of the CMB solar dipole (3364.3 ± 1.5 μK), which is approximately 1σ higher than the WMAP measurement with a direction that is consistent between the two experiments. We describe the pipeline used to produce the maps of intensity and linear polarization from the HFI timelines, and the scheme used to set the zero level of the maps a posteriori. We also summarize the noise characteristics of the HFI maps in the 2015 *Planck* data release and present some null tests to assess their quality. Finally, we discuss the major systematic effects and in particular the leakage induced by flux mismatch between the detectors that leads to spurious polarization signal.

Key words. cosmology: observations – cosmic background radiation – surveys – methods: data analysis

---

1. Introduction

This paper, one of a series associated with the 2015 *Planck* data release, is the second of two describing the processing of the data from the High Frequency Instrument (HFI). The HFI is one of the two instruments on board *Planck*[1], the European Space Agency's satellite dedicated to precision measurements of the cosmic microwave background (CMB). The HFI uses cold optics (at 4 K, 1.6 K, and 100 mK), filters, and 52 bolometers cooled to 100 mK. Coupled with the *Planck* telescope, it enables us to map the continuum emission of the sky in intensity and polarization at frequencies of 100, 143, 217, and 353 GHz, and in intensity at 545 and 857 GHz. Paper A (Planck Collaboration VII 2016) describes the processing of the data at the time-ordered level and the measurement of the beam. Paper B (this paper) describes the HFI photometric calibration and mapmaking.

Paper A describes how the time-ordered information (TOI) of each of the 52 bolometers is processed and flagged. Sampled at 5.544 ms, the TOI is first corrected for the analog-to-digital converter (ADC) non-linearity, then it is demodulated and converted to the absorbed power with a simple non-linear bolometric correction. Glitches are flagged and glitch tails are removed from the TOI. Thermal fluctuations are removed on the 1 min timescale. Sharp lines in the temporal power spectrum of the TOI from the influence of the 4-K cooler are removed. Finally, the bolometer time response is deconvolved and the TOI is low-pass filtered. At this point, the TOIs are cleaned but not yet calibrated. The measurement of the beam is performed using a combination of observations of planets for the main beam and GRASP[2] physical optics calculations for the sidelobes. The focal plane geometry, or the relative position of bolometers in the sky, is deduced from Mars observations.

This paper describes how the prepared TOIs are used to make the calibrated maps for all *Planck* HFI bands. After a summary of the photometric definitions (Sect. 2), this paper gives a description of the main steps of the mapmaking processing, focusing on the changes made since the previous *Planck* releases (Planck Collaboration VI 2014; Planck HFI Core Team 2011). The major difference concerns the calibration (Sect. 3), which is now based on the orbital CMB dipole for the lower frequency channels (100, 143, 217, and 353 GHz, also called CMB channels) while the 545 and 857 GHz channels are photometrically calibrated using the signal from Uranus and Neptune. Section 4 explains the mapmaking upgrades, including the polarization treatment. Section 5 describes the maps, the solar dipole measurement, and the derivation of far sidelobes and zodiacal maps. Section 6 presents the noise characteristics and the null tests obtained by splitting the *Planck* HFI dataset into different groups based on ring period, time period, or detector sets. Consistency checks are performed in order to assess the fidelity of the maps. Finally, Sect. 7 is dedicated to the description of systematic effects, in particular in polarization. The major systematic residuals in *Planck* HFI data are due to the leakage from temperature to polarization induced by flux mismatch between associated bolometers. This is the result of either bandpass mismatch, or zero-level uncertainty, or calibration uncertainty. We present a

first attempt to correct the maps for the intensity-to-polarization leakage. At lower frequencies, even after correction, the residuals are still higher than the noise level and thus the maps cannot yet be used for cosmological analysis.

2. Photometric equations

The power absorbed by a given detector at time t can be written as the sum of three terms corresponding to the first three Stokes parameters (I_p, Q_p, U_p) at the sampled pixel p of the beam-convolved sky,

$$P_t = G \left[I_p + \rho \left\{ Q_p \cos 2(\psi_t + \alpha) + U_p \sin 2(\psi_t + \alpha) \right\} \right] + n_t, \quad (1)$$

where G encodes a photometric calibration factor, ρ is the detector polarization efficiency, ψ_t is the roll angle of the satellite, α is the detector polarization angle, and n_t represents all the noise contributions to the absorbed power (photon noise, phonon noise, glitch residuals, etc.). The polarization efficiency is derived from the cross-polarization coefficient η through $\rho = (1 - \eta)/(1 + \eta)$. It allows us to describe spider-web bolometers (SWB, $\rho \approx 0$) as well as polarization-sensitive bolometers (PSB, $\rho \approx 1$). According to the bolometer model and given the stability of the HFI operational conditions during the mission, the gain G is expected to be constant over the whole mission (see Sect. 1 of Paper A) once the bolometer non-linearities have been corrected.

For an axisymmetric beam response, the "smearing" and "pointing" operations commute, and one can solve directly for the pixelized beam-convolved map,

$$P_t = G \left(1, \rho \cos 2(\psi_t + \alpha), \rho \sin 2(\psi_t + \alpha) \right)^\dagger \cdot \left(I_p, Q_p, U_p \right) + n_t$$
$$\equiv G \times A_{tp} T_p + n_t, \quad (2)$$

where the direction of observation at the time t, (θ_t, ϕ_t), falls into pixel p and we define the map-pointing matrix A and the sky signal $\boldsymbol{T} = (I, Q, U)$.

3. Calibration

The bolometer signal measured through current-biasing is proportional to the small variation in the incoming power from the sky. To express the measurement in sky temperature units, one has to determine a gain per detector based on a known source in the sky. For the HFI low-frequency channels (100 to 353 GHz), we use the CMB orbital dipole as a primary calibrator. This signal fills the entire beam and is almost insensitive to the beam profile and only marginally affected by pointing errors, while its signal-to-noise is high enough thanks to the full-sky coverage. Moreover, it is a stronger signal than CMB anisotropies (by a factor of around 10), but not bright enough to cause non-linearities in the detectors, and has the same electromagnetic spectrum as the anisotropies. At higher frequencies (545 and 857 GHz), calibration is performed on planets.

3.1. CMB dipole conventions

The CMB dipole is induced by the Doppler effect of the relative motion of the satellite with respect to the CMB frame,

$$T_{\mathrm{Doppler}}(t, \hat{\boldsymbol{u}}) = \frac{T_{\mathrm{CMB}}}{\gamma_t (1 - \boldsymbol{\beta}_t \cdot \hat{\boldsymbol{u}})}, \quad (3)$$

where $\boldsymbol{\beta}_t = \boldsymbol{v}_t/c$ and $\gamma_t = (1 - \beta_t^2)^{-1/2}$, $\boldsymbol{v}_t$ is the satellite velocity at time t, and $\hat{\boldsymbol{u}}$ is the unit vector along the line of sight.

The solar system motion with respect to the CMB frame, giving rise to what is referred to as the solar dipole, is the dominant component of the satellite velocity. A residual contribution (called the orbital dipole) is induced by the yearly motion of the satellite with respect to the solar system barycentre. The solar dipole can be considered as sky-stationary during the observations and is thus projected onto the sky as an $\ell = 1$ component with amplitude previously measured by COBE and WMAP, $3355 \pm 8\,\mu$K (Hinshaw et al. 2009). Relativistic corrections to the solar dipole produce second-order anisotropies at multipoles $\ell \geq 1$ with amplitudes proportional to β^ℓ and, more importantly, couple the two dipole components, as will be discussed below. Although the orbital dipole velocity is typically an order of magnitude lower than the solar dipole, it is time dependent and its time-variability is precisely determined by the satellite velocity, which is known at the level of 10^{-4} km s^{-1}. Finally, to calibrate in temperature, we only rely on an external measurement of the CMB absolute temperature. We use $T_{CMB} = 2.7255$ K (Fixsen 2009).

The expansion of Eq. (3) in β gives

$$\Delta(\hat{\boldsymbol{u}}) = \frac{T_{Doppler}}{T_{CMB}} - 1 \approx \boldsymbol{\beta} \cdot \hat{\boldsymbol{u}} - \frac{\beta^2}{2} + (\boldsymbol{\beta} \cdot \hat{\boldsymbol{u}})^2 + O\left(\beta^3\right). \tag{4}$$

If we decompose the velocity into a *solar* boost $\boldsymbol{\beta}_1$ and an *orbital* boost $\boldsymbol{\beta}_2$ then

$$\Delta = \Delta_1 + \Delta_2 - \boldsymbol{\beta}_1 \cdot \boldsymbol{\beta}_2 + 2(\boldsymbol{\beta}_1 \cdot \hat{\boldsymbol{u}})(\boldsymbol{\beta}_2 \cdot \hat{\boldsymbol{u}}) + O\left(\beta^3\right), \tag{5}$$

where the first term corresponds to the solar dipole, the second term is the orbital dipole, and the third and fourth terms show the coupling between each term due to relativistic corrections.

3.2. Absolute calibration on orbital dipole

The calibration algorithm takes advantage of the orbital dipole not being fixed on the sky, unlike the solar dipole (during the length of the mission). In practice, relativistic corrections and second order in the development of the conversion from I_ν to T_{cmb} couple solar and orbital dipoles creating an additional non-stationary signal, which also depends on the frequency. We use the total CMB dipole computed using Eq. (3) as the calibration reference signal, assuming that it has the same scaling with frequency as the higher multipole CMB anisotropies. This approximation will leave in the HFI frequency maps the frequency dependent fraction of the kinematic quadrupole arising from the second-order term in the β expansion described in Kamionkowski & Knox (2003) and Quartin & Notari (2015). The amplitude of the kinematic quadrupole is expected to be lower than 0.5% on the CMB-calibrated *Planck*-HFI channels. However, it is not directly correlated to the orbital dipole on which we calibrate the data. Thus, we expect the systematic error induced on the gain estimation to be much smaller.

The orbital dipole signal is modulated on a one-year period. To take into account the time variation of this signal, we need to add a term in Eq. (2),

$$\boldsymbol{P} = G \times (A\boldsymbol{T} + \boldsymbol{t}_{orb}) + \boldsymbol{n}, \tag{6}$$

where $\boldsymbol{t}_{orb}$ is the time-dependent orbital dipole signal, while in this formula the solar dipole is part of the sky signal $\boldsymbol{T}$. We note that we can arbitrarily set all or part of the solar dipole signal either in the calibration template or in the sky without changing the resulting gain estimation.

Since $\boldsymbol{t}_{orb}$ is known, we can solve Eq. (6) for each bolometer independently, rewriting the system as

$$\boldsymbol{P} = A\tilde{\boldsymbol{T}} + G\boldsymbol{t}_{orb} + \boldsymbol{n}, \tag{7}$$

where the unknowns are the sky-signal in absorbed power units $\tilde{\boldsymbol{T}}$ and the gain G. The calibration problem is thus linear and can be solved directly. The maximum-likelihood estimate of the gain G is obtained by combining all available samples using the noise covariance matrix $N = \langle n^\dagger n \rangle$ and marginalizing over $\tilde{\boldsymbol{T}}$, solving the equation

$$\left(\boldsymbol{t}_{orb}^T N^{-1} Z \boldsymbol{t}_{orb}\right) \times G = \boldsymbol{t}_{orb}^T N^{-1} Z \boldsymbol{d}, \tag{8}$$

where $\boldsymbol{d}$ is the vector of input data P_t and we define

$$Z = I - A\left(A^T N^{-1} A\right)^{-1} A^T N^{-1}. \tag{9}$$

In practice, the noise is treated by assuming that the destriping reduces the matrix N to a diagonal one once the data $\boldsymbol{d}$ have been corrected for a constant offset (see Sect. 4.2). For the HFI, the mapmaking problem is degenerate for the reconstruction of polarization if we solve for a single detector at a time. Neglecting polarization in Eq. (8) for polarization-sensitive detectors biases the calibration solution. Moreover, we need a very accurate relative calibration between detectors that are combined to reconstruct polarization in order to minimize leakage from intensity to polarization (see Sect. 7.3). For this reason, for the *Planck* 2015 release we have extended the algorithm described in Tristram et al. (2011) to perform a multi-detector gain estimation for all bolometers at a given frequency together with the offsets (see Sect. 4.2).

3.3. Long time-constant residuals

The observation strategy of Planck results in the path across a particular part of the sky being almost reversed six months later. As described in Paper A, we take advantage of this to derive the time transfer function below one second. Nevertheless, longer time responses (larger than the second), even with low amplitudes, may bias the calibration estimation by distorting the dipole signal and causing some leakage of the solar into the orbital dipole. To take into account the systematic residuals after time-constant deconvolution into account, we built a simplified model describing a pure single-mode sinusoidal dipole signal (including solar and orbital dipole) convolved with an exponential decay in the time domain. In the frequency domain, this reads

$$\mathcal{T}_{dip} = \mathcal{F}\left(t_{dip} * Be^{-t/\tau}\right) = \frac{B}{1/\tau + 2i\pi\nu}\delta_{\nu,\nu_{spin}}, \tag{10}$$

where B and τ are the amplitude and the time constant, and ν_{spin} is the spin frequency; $\mathcal{T}_{dip}$ is a complex coefficient, the real part of which corresponds to the relative change in the gain G, while the imaginary part corresponds to the amplitude of the dipole mode shifted by 90°.

In practice, prior to the absolute calibration, we solve for the amplitude of a shifted-dipole template using single detector calibration,

$$\boldsymbol{P} = A\tilde{\boldsymbol{T}} + G\boldsymbol{t}_{dip} + C\boldsymbol{t}_{dip}^{90°} + \boldsymbol{n}, \tag{11}$$

where C gives the amplitude of the dipole mode shifted by 90°. With this toy model, we cannot reconstruct the amplitude and the time constant because we only fit for one coefficient C, but we trace the systematic effect on the dipoles due to the very long
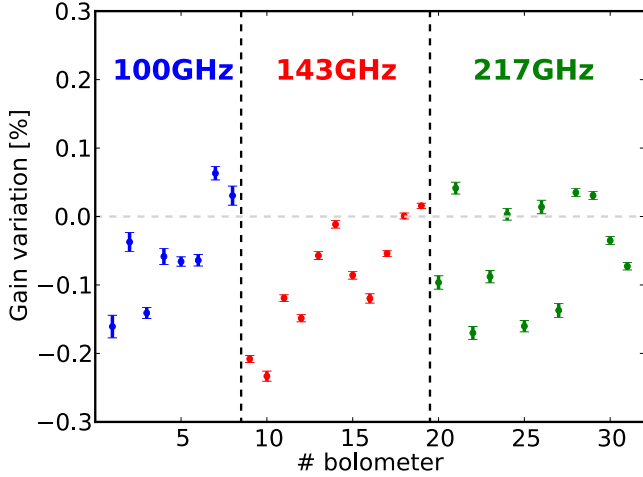
Fig. 1. Effect on the gains when including the model for long time constant residuals as described in the text.

time response. Once the coefficient C has been determined, we correct the data for $Ct_{\mathrm{dip}}^{90°}$ to account for this additional shifted mode coming from the residual time constant.

The effect on the gain G depends on the unknown value of the time constant τ. Figure 1 shows the impact on the gains for each bolometer when including the shifted-dipole correction. At higher frequencies (353 GHz and above), the signal is no longer dominated by a dipole and cannot be approximated by the model described above. For the 2015 release, we do not include any correction for time constant residuals in the mapmaking for those channels.

3.4. Submillimetre calibration

Mars, Jupiter, Saturn, Uranus, and Neptune are all observed several times during the full length of the mission. The submillimetre channels of HFI (545 and 857 GHz) are calibrated on models of Uranus and Neptune. We do not use Jupiter and Saturn observations for calibration since both planets have strong absorption features at those frequencies, which complicate comparison with broadband measurements. The flux from Jupiter also leads to detector saturation at the highest HFI frequencies. Similarly, we choose not to use Mars as a calibrator because strong seasonal variations complicate the modelling.

Various methods are used to derive planet flux densities, including aperture photometry and point-spread function (PSF) fits. Planet measurements with *Planck* are studied fully in Planck Collaboration XXXIV (in prep.). We focus here on calibration using aperture photometry in the time-ordered data from the submillimetre channels. The simulation pipeline used for the main beam reconstruction computes the reconstruction bias and the error budget (the mean and the variance) for each planet observation. The comparison of flux measurements of Neptune and Uranus with up-to-date models provides the calibration factors at 545 and 857 GHz.

3.4.1. Planet models

We use the ESA 2 model for Uranus and the ESA 3 model for Neptune (Moreno 2010). Both models quote absolute uncertainties of 5%. Planet model spectra are produced from their modelled brightness temperatures using the planet solid angles at the time of observation and integrated under the
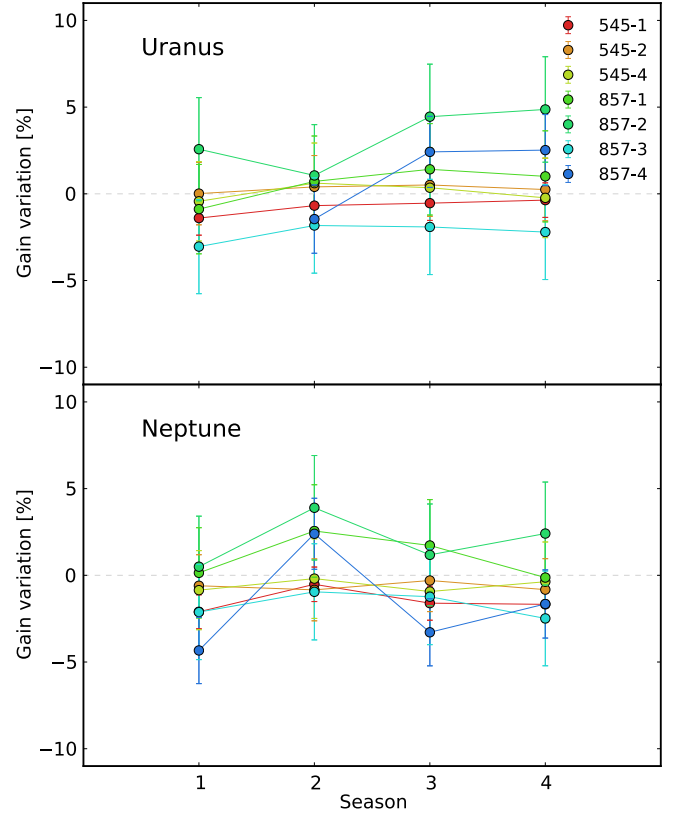

Fig. 2. Dispersion of the planet-derived calibration factor per season around the planet calibration estimates for Uranus (*top*) and Neptune (*bottom*).

individual 545 and 857 GHz bolometer bandpasses. Flux densities are colour-corrected to a reference spectrum defined by a constant νI_ν law so as to be directly comparable to HFI flux density measurements.

Planck Collaboration XXXIV (in prep.) gives a detailed account of the ratio between the expected planet fluxes and the measured values at all HFI frequencies and for the five observed planets (Mars, Jupiter, Saturn, Uranus, and Neptune). They all fall within the 5% model uncertainty range. This is a validation of the models at 100–353 GHz. Hence the models can be used with some confidence to calibrate the 545 and 857 GHz channels.

3.4.2. Aperture photometry in the timelines

We select all samples in a $2° \times 2°$ box around the planet positions and build time-ordered vector objects (hereafter timelines) for each bolometer and each planet scan. We use the first four scans of Neptune and Uranus (season 1 to 4). We build corresponding background timelines using all the samples in a $2° \times 2°$ box around the planet position when the planet is not there. The resulting background has a much higher spatial density than the planet timelines. We use this to build a background mini-map with $2' \times 2'$ pixels that can then be interpolated at each sample position in the planet timelines in order to remove a local background estimate (see Appendix B in Paper A for details).

The aperture photometry measurement procedure applied to our planet timelines is an extension of the usual aperture photometry approach to irregularly gridded data. Flux is integrated in an aperture of radius 3 times the effective FWHM. Typically, aperture photometry is applied to maps of fixed-size pixels,
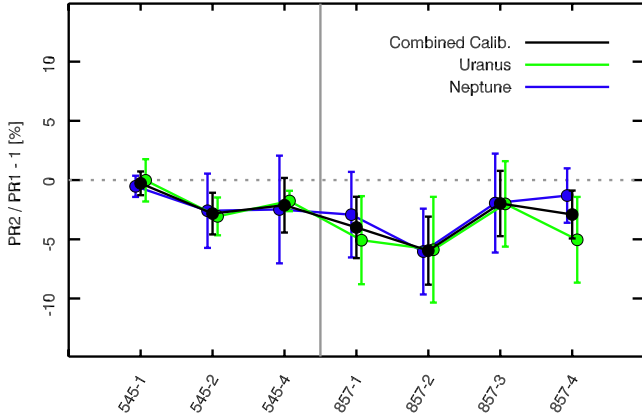
Fig. 3. Comparison of the 2015 *Planck* release calibration to the 2013 release. We show the relative difference in percent per bolometer for Uranus (green), Neptune (blue), and both calibrators combined (black).

Table 1. Uncertainties in the planet-derived calibration factor for each bolometer.

Bolometer	Uncertainty stat.	Uncertainty syst.
545-1	1.0%	5.0%
545-2	1.8%	5.0%
545-4	2.3%	5.0%
857-1	2.6%	5.0%
857-2	2.9%	5.0%
857-3	2.8%	5.0%
857-4	2.0%	5.0%

Notes. The systematic uncertainty is the absolute uncertainty of the planet model.

which means integrating the flux in the aperture is equivalent to summing the pixel values. In our case, we have to take into account the inhomogenous spatial distribution of the samples. To do this we assume that the beam products perfectly describe the spatial light profile of Neptune and Uranus, and compute a spatial sampling correction factor as the ratio of the integrated flux in a highly spatially oversampled beam and the integrated flux in a beam sampled on the planet timelines. This sampling correction has to be computed for each bolometer and planet crossing, because the spatial sampling varies between planet observations. We estimate the statistical uncertainty of the measurements as the standard deviation of the samples in an annulus of radius 3 to 5 times the effective FWHM of the beam.

We find large variations between the individual planet measurements in each detector and at each season of the full mission survey (Fig. 2) which we attribute to the underestimation of the measurement uncertainty. The signal from Neptune and Uranus is not expected to vary in time apart from the differences in solid angle which are very small and already taken into account. While accurately corrected by the timeline aperture photometry algorithm presented here, the limited available spatial sampling of the planet signal at these frequencies could explain part of the variations. We therefore decided to include the seasonal root mean square (rms) of the measurements (we have four observations per bolometer per planet) in the measurement uncertainty.

The averaged calibration factors for each detector for each planet are in very good agreement. The final calibration factors are the means of both planet estimates. We compare them to the 2013 *Planck* release in Fig. 3: the calibration factors changed by 1.9 and 4.1% at 545 and 857 GHz, respectively, which is within the planet modelling uncertainty. Combined with other pipeline changes (such as the analog-to-digital converter non-linearity corrections), the 2015 frequency maps have decreased in brightness by 1.8 and 3.3% compared to 2013.

Calibration uncertainties are given in Table 1. In order to produce the frequency maps, detectors are weighted by their inverse noise variance. We use the same weights to compute the corresponding calibration errors. We estimate combined statistical errors of 1.1% and 1.4% at 545 and 857 GHz, respectively, to which one should add linearly (as should be done for systematics) the 5% uncertainty arising from the planet models. Errors on absolute calibration are therefore 6.1 and 6.4% at 545 and 857 GHz, respectively. Since the reported relative uncertainty of the models is of the order of 2%, we find the relative

calibration between the two HFI highest frequency channels to be better than 3%.

4. Mapmaking

4.1. Summary

Each data sample is calibrated in K_{CMB} for the 100, 143, 217, and 353 GHz channels, or MJy sr^{-1} (assuming a constant νI_ν law) for the 545 and 857 GHz channels, using the calibration scheme described above. The bolometer gains are assumed to be constant throughout the mission, which was not the case for the 2013 release. The *Planck* total dipole (solar and orbital) is computed and subtracted from the data.

As in the *Planck* 2013 release, we average the measurements for each detector in each pixel visited during a stable pointing period (hereafter called a ring) while keeping track of the bolometer orientation on the sky. The subsequent calibration and mapmaking operations use this intermediate product as input. The calibrated TOIs are only modified by a single offset value per ring and per detector. The offsets are determined with the destriping method described in Tristram et al. (2011). Here, the size of the pixels where the consistency of different rings is tested is 8′ (N_{side} = 512). Maps in intensity and polarization are used to assess the consistency of the destriper solution. The offsets are simultaneously determined for all bolometers at a given frequency using the full mission data. For all the maps produced using a given bolometer, the same offset per ring is used (except in the case of half-rings, see below).

The products of the HFI mapmaking pipelines are maps of I, Q, U together with their covariances (II, IQ, IU, QQ, QU, UU), pixelized according to the HEALPix scheme (Górski et al. 2005). The map resolution is N_{side} = 2048, and the pixel size is 1′.7. The mapmaking method is a simple projection of each unflagged sample to the nearest grid pixel. In the case of polarization data with several detectors solved simultaneously, the polarization equation is inverted on a per-pixel basis (see Sect. 4.2). For each sky map, a hit count map is computed (number of samples per pixel; one sample has a duration of 5.544 ms).

The zodiacal light component, which varies in time, is estimated using templates fitted on the survey-difference maps (see Sect. 5.4). We provide maps without zodiacal light for which these templates are systematically subtracted from the data of each bolometer prior to the mapmaking.

Unlike in the 2013 release, the far sidelobes are not removed from the maps. At most, this leaves residuals of the order of 0.5–1.5 μK in the 100–353 GHz maps with uncertainties on the residuals of roughly 100% (Planck Collaboration VII 2016).

At higher frequencies, Galactic pick-up from the far sidelobes produces significant residuals in about half of the detectors of the order of 0.03 MJy sr^{-1} at 545 and 0.3 MJy sr^{-1} at 857 GHz (see Planck Collaboration X 2016). The total solid angle in the spillover is a better known quantity, and we describe the effect of the far sidelobes on the calibration in Sect. 5.3.

4.2. Mapmaking method

In the same way as in Planck Collaboration VIII (2014), we use a destriping algorithm to deal with the HFI low-frequency noise. In this approach, the noise in a ring r is represented by an offset, denoted o_r, and a white noise part n, which is uncorrelated with the low-frequency noise. For a given bolometer, we can write Eq. (6) as

$$P_t = G \times (A_{tp} T_p + t_{orb}) + \Gamma_{tr} o_r + n_t, \qquad (12)$$

where Γ_{tr} is the ring-pointing matrix (which associates the data sample t with the ring number r). The unknowns are the gain G, the offsets for each ring o_r, and the sky signal for each pixel $T_p = (I_p, Q_p, U_p)$. As there is a degeneracy between the average of the offsets and the zero level of the maps, we impose the constraint $\langle o_r \rangle = 0$. The absolute zero level of the maps is determined as described in Sect. 4.4.

For the production of the maps for the 2015 HFI data release, we first build the rings for all detectors. We apply the following frequency-dependent processing to these compressed data sets.

For CMB frequencies (100, 143, and 217 GHz) channels we proceed as follows:

1. we estimate a first approximation of the orbital dipole gain together with the offsets and the amplitude of the long-time-constant residuals for each bolometer independently, neglecting the polarization signal;
2. we then derive the gains and offsets for a fixed amplitude of the long-time-constant residuals using the multi-bolometer algorithm.

At 353 GHz, the long-time-constant residuals are more difficult to constrain. They are driven more by Galactic emission drifts than by the dipole, which dominates at lower frequencies, so that the model described in Sect. 3.3 is not relevant. Hence for this frequency we use a simpler pipeline without a long-time-constant residuals template:

1. we estimate the orbital dipole gain together with the offsets for each bolometer independently, neglecting the polarization signal;
2. we then estimate the final offsets using a destriping procedure for all bolometers at this frequency.

For the two highest frequencies, at 545 and 857 GHz, the pipeline is considerably different because we use the planets (Uranus and Neptune) as calibration sources:

1. we estimate a first approximation of the offsets for each bolometer independently;
2. we derive the gains from the planet flux comparison;
3. we then estimate the final offsets with a destriping procedure for all bolometers at a given frequency.

Finally, using the pre-computed gains and offsets, we project the ring data onto maps for each data set. For polarization, we invert the 3×3 system derived from Eq. (12) for each pixel independently with the criterion that the condition number be lower

than 10^3,

$$T = \left(A^T N^{-1} A\right)^{-1} A^T N^{-1} d, \qquad (13)$$

where d are the calibrated, cleaned ring data (offsets and orbital dipole removed) $d = (P - \Gamma o)/G - t_{orb}$. We note that we use HEALPix (not IAU) conventions for the sign and normalization of the Q and U Stokes parameters.

For destriping, we use the same tool as before, polkapix, which was thoroughly validated in Tristram et al. (2011). Maps are built by simple co-addition in each pixel of the destriped, calibrated, and time-varying component-subtracted signal. We subtract the CMB dipole as measured by *Planck* (see Sect. 5.1).

We introduced the following modifications with respect to Planck Collaboration VIII (2014):

– we included polarization in the destriping for the channels that include polarization-sensitive bolometers;
– we enlarged the masked fraction of the sky from 10 to 15%, based on Galactic emission, to avoid signal gradients leaking into offsets;
– to improve the offset accuracy, we computed one set of offsets combining all detectors, using full-mission data, and used them for all derived maps involving these detectors.

This last change induces a small noise correlation between detector-set maps (see Sect. 6.5). In 2013 we computed independent offsets for each detector or detector set, including the full mission.

4.3. Map products

The principal HFI final product consists of six maps that cover the six frequencies (100–857 GHz) for the full mission in intensity at high resolution ($N_{side} = 2048$). However, many more maps are needed to assess the noise and the consistency of the data. Figure 4 summarizes the various splits produced. The branches that are delivered in the 2015 release are described in Appendix A.

Maps from different halves of each ring period (first and last) are computed independently of each other, including the offset per half-ring. Thus, half-ring half-difference maps can give a quick account of the noise level in the maps.

For each frequency, we also produce temperature and polarization maps using detector sets (each set including four polarization-sensitive bolometers). In addition, we produce a temperature map for each spider-web bolometer.

The *Planck* scanning strategy samples almost all the sky pixels every six months, with alternating scan directions in successive six-month periods. The full cold HFI mission encompasses five surveys, each covering a large fraction of the sky. Surveys 1–2 and 3–4 are paired to produce Year 1 and Year 2 maps (see Table A.2). Maps are produced for the full-mission dataset together with the survey, year, and half-mission maps. Each map is associated with a hit-count map and variance maps (II; and QQ, UU, IQ, IU, and QU when polarization is reconstructed). Overall, a total of about 6500 sky maps have been produced. We have used this data set to evaluate the performance of the photometric calibration by examining difference maps (see Sect. 6.2).

4.4. Zero levels

Planck-HFI cannot measure the absolute sky background. The mapmaking procedure does not change the mean value of the
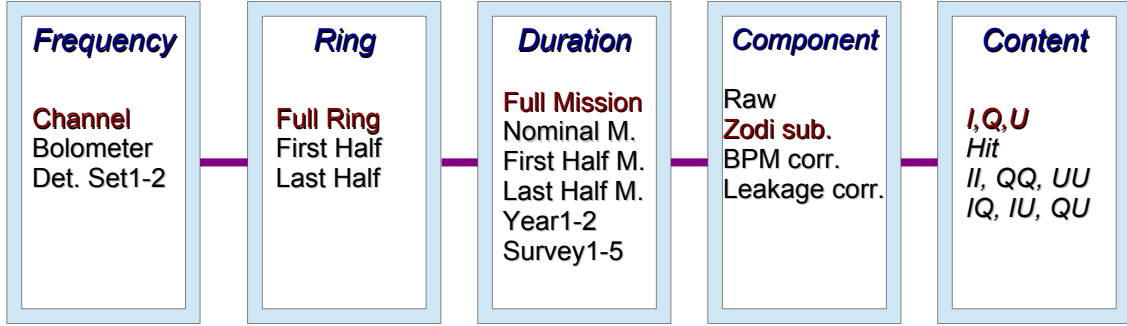
Fig. 4. Map matrix. The HFI maps are released in different flavours. Not all combinations are released, but any map will correspond to a choice of lines in each box. The *Frequency* box is related to the use of all detectors at a given frequency (Channel), or individual bolometers, or sets of detectors as defined in Table A.1. The *Ring* box is a way of splitting (or not) the data in equal halves at the ring level. The *Duration* box indicates the different ways of splitting data between surveys: years, full or nominal mission, first half mission, or last half mission. The *Component* box indicates the systematic corrections that can be applied at the map level. The recommended first choice map is highlighted in red. See Appendix A for details.

Table 2. CMB solar dipole measurements for the 100 and 143 GHz channels estimated for different sky coverage levels (37, 50, and 58%) corresponding to three thresholds in 857 GHz amplitude (2, 3, and 4 MJy sr^{-1}).

Frequency [GHz]	Threshold [MJy sr^{-1}]	d [μK]	Lon [°]	Lat [°]
100	2	3364.81 ± 0.06	263.921 ± 0.002	48.2642 ± 0.0008
100	3	3364.76 ± 0.05	263.922 ± 0.002	48.2640 ± 0.0006
100	4	3364.99 ± 0.04	263.928 ± 0.002	48.2631 ± 0.0006
143	2	3364.05 ± 0.03	263.908 ± 0.001	48.2641 ± 0.0004
143	3	3363.72 ± 0.02	263.903 ± 0.001	48.2653 ± 0.0003
143	4	3363.39 ± 0.02	263.905 ± 0.001	48.2668 ± 0.0003

Notes. Uncertainties include only statistical errors. Systematic errors are $0.8\,\mu$K for the amplitude, and (0°024, 0°0034) in Galactic (longitude, latitude).

input TOI. We therefore adjust the monopole on the maps a posteriori in a similar manner to the method used in Planck Collaboration VIII (2014), which relies on external datasets. To achieve this, we need to take into account two major components of the monopole:

1. Galactic dust emission: we estimate the brightness in the HFI single-detector maps that corresponds to zero gas column-density (i.e. zero Galactic dust emission) by using the H I column density, which is assumed to be a reliable tracer of the Galactic gas column-density in very diffuse areas (see Planck Collaboration VIII 2014, Sect. 5.1). The offsets derived are then subtracted from each detector's data in the processing.
2. Extragalactic emission: the cosmic infrared background (CIB) monopole is taken into account by adding the levels from Béthermin et al. (2012) to the maps (see Table 6).

The sum of the two offsets is appropriate for total emission analysis. For Galactic studies, only the Galactic zero level has to be set which can be achieved by subtracting the CIB levels (Table 6) from the released maps. Unlike the previous release, in the 2015 maps the zero-level correction (both CIB and Galactic) has been applied.

Zodiacal light has not been accounted for in this procedure. The correction to be applied at each frequency to set the Galactic zero level using zodiacal-light-corrected maps are given in Table 6.

4.5. Polarization efficiency and orientation

The *Planck*-HFI bolometers were characterized on the ground before launch. Rosset et al. (2010) reported pre-flight measurements of the polarization efficiency of the HFI polarization-sensitive bolometers with an accuracy of 0.3%. The absolute orientation of the focal plane was measured at a level better than 0°3. The relative orientation between bolometers is known with an accuracy better than 0°9.

Spider-Web Bolometers are much less sensitive to polarization. Nonetheless, we take into account their polarization efficiency, which is between 1 and 9%, although their orientations have been less accurately determined (errors can be up to a few percent), as described in Rosset et al. (2010).

5. HFI temperature and polarization maps

5.1. Solar dipole measurement

The $\ell = 1$ mode of CMB anisotropy is unique in that its amplitude is dominated by a large component associated with our motion with respect to the CMB rest frame. In this section, we present the CMB solar dipole results based on *Planck*-HFI maps at the two lowest frequencies, 100 and 143 GHz. Low-frequency maps are dominated by CMB over a large fraction of the sky. Nevertheless, the inhomogeneous nature of the dust emission can bias CMB solar dipole estimates.

We cleaned the Galactic emission from the HFI maps using a local correlation with the 857 GHz map. We model each

HFI map I_ν as

$$I_\nu - C = qI_{857} + D_{\text{res}}, \tag{14}$$

where C is the CMB anisotropy (here we use the SMICA map, Planck Collaboration IX 2016, from which we remove any residual dipole component) and I_{857} is the *Planck* 857 GHz map that is assumed to have a negligible contribution from the solar dipole[3]. The term D_{res} includes the dipole and any systematic effects from both I_{857} and I_ν. In bright regions of the sky, D_{res} also contains extra emission that is uncorrelated or only partially correlated with I_{857}, for instance free-free emission or CO.

In order to capture any spatial variations of the dust spectral energy distribution (SED), we estimated q and D_{res} on an $N_{\text{side}} = 64$ grid. For each $N_{\text{side}} = 64$ pixel, we performed a linear regression of the $N_{\text{side}} = 2048$ pixels of I_ν vs. I_{857}, assuming a constant dust SED over a 55′ area. We then fit for the dipole amplitude and direction in D_{res} using sky pixels where $I_{857} < 2$, 3, or 4 MJy sr^{-1} (corresponding to 37, 50, or 58% of the sky respectively) to limit the effect of Galactic-emission residuals (CO, free-free emission, and small-scale dust SED variations).

The results are given in Table 2. We measure a solar system peculiar velocity of 370.06 ± 0.09 km s^{-1} with respect to the CMB rest frame. We use the CMB temperature from Fixsen (2009; 2.7255 ± 0.0006 K) to convert that measurement into a CMB dipole measurement.

The error bars here only include statistical uncertainties, which are very low thanks to the *Planck*-HFI signal-to-noise ratio. We evaluate the additional systematic uncertainties from the variation of the results between independent bolometer maps. For the amplitude, the peak-to-peak variation between bolometers and combined maps is $\pm 0.8\,\mu$K at 100 and 143 GHz. Variations with sky coverage are of the same order. We note that the uncertainty from the FIRAS temperature should be added to the budget ($\pm 0.74\,\mu$K). For the coordinates, we found variations of $\pm 0°013$ in longitude and $\pm 0°0019$ in latitude. These differences are observed when comparing results at different frequencies, and are likely to result from uncertainties in the foreground subtraction. This is also consistent with the magnitude of the direction shifts we observe when changing the sky fraction.

As an independent check, we also produce a cleaned CMB map using an internal linear combination (ILC) method. We used the HFI maps at 100, 143, and 217 GHz smoothed with a 1° FWHM Gaussian kernel. We note that smoothing the data with a 1° kernel reduces the solar dipole in the maps by 0.005%, i.e. $0.2\,\mu$K, which we corrected for afterwards. We then estimate the solar dipole amplitude and direction using a Galactic mask that removes less than 15% of the sky to avoid the inner Galactic plane where the residuals are most intense. The measurement is compatible with the results in Table 2.

In the end, the amplitude (d) and direction (Galactic longitude, latitude) of the solar dipole measured by *Planck*-HFI is

$$d = 3364.29 \pm 0.02(\text{stat}) \pm 0.8(\text{sys}) \pm 0.74(\text{FIRAS})\ \mu\text{K}$$

$$\begin{pmatrix} \text{lon} \\ \text{lat} \end{pmatrix} = \begin{pmatrix} 263°914 \pm 0°001\ (\text{stat}) \pm 0°013\ (\text{sys}) \\ 48°2646 \pm 0°0003(\text{stat}) \pm 0°0019(\text{sys}) \end{pmatrix}.$$

This is to be compared to the official *Planck* solar dipole measurement obtained in combination with the *Planck*-LFI:

$$d = 3364.5 \pm 2.0\ \mu\text{K}$$

$$\begin{pmatrix} \text{lon} \\ \text{lat} \end{pmatrix} = \begin{pmatrix} 264°00 \pm 0°03 \\ 48°24 \pm 0°02 \end{pmatrix}.$$

---

[3] The amplitude of the solar dipole at 857 GHz is 0.0076 MJy sr^{-1}. At least 90% of this is removed in the mapmaking process, leaving a residual that is well below the noise level and any systematic effects.

Compared to the WMAP five-year results $(d, \text{lon}, \text{lat}) = (3355 \pm 8\ \mu\text{K}, 263°99 \pm 0°14, 48°26 \pm 0°03$; Hinshaw et al. 2009), this is $9.3\,\mu$K (0.28%) higher in amplitude while shifted by $(0'6, 1'2)$ in longitude and latitude. Part of the difference ($0.6\,\mu$K) is due to the revised CMB monopole temperature compared to Mather et al. (1999; 2.725 K). This total dipole (solar, orbital, relativistic, and interactions thereof) is removed from the calibrated TOI before final mapmaking.

5.2. Planck-HFI maps

Frequency maps have been produced using inverse noise weighting. In Figs. 5 and 6 we show the six intensity frequency maps from 100 to 857 GHz at full resolution ($N_{\text{side}} = 2048$). Figure 7 presents polarization maps at the first four frequencies (100, 143, 217, and 353 GHz), degraded to lower resolution ($N_{\text{side}} = 256$) in order to enhance the signal-to-noise ratio. These maps have been corrected from bandpass leakage as will be discussed in Sect. 7.3.1. In both intensity and polarization, we clearly see the emission from the Galactic dust increasing with frequency. In intensity, CMB anisotropies are visible at high latitude in the low-frequency channels (between 100 and 217 GHz). In polarization, the 100 GHz maps are contaminated in the Galactic plane by residual CO leakage coming from bandpass mismatch between bolometers.

5.3. Far sidelobes

As noted in Planck Collaboration VII (2016), far sidelobes affect the response of the instrument to large-scale structures. In addition, the far sidelobes also affect the HFI calibration.

At low frequencies, HFI calibrates by fitting to the sinusoidal signal created by the dipole modulated by the *Planck* circular scanning strategy. As outlined in Appendix B of Planck Collaboration XXXI (2014), this effectively weights different parts of the beam in general, and the sidelobes in particular, by their angle from the spin-axis. For example, far sidelobe contributions close to the spin-axis actually affect the calibration very little. Similarly, since we are calibrating with signals that are "in phase" with the known phase of the main beam as it scans, the further a sidelobe contribution is in angle *around* the spin-axis from the main lobe, the less it contributes to the calibration. So, a sidelobe contribution that is 90° in scan phase from the main lobe, for example, would not contribute to the HFI calibration, while something close to the main beam would potentially have a large effect. The change of the gain due to the far sidelobes is calculated by fitting the dipole to full timeline simulations of the dipole convolved by the far sidelobes. The factors are 0.09% at 100 GHz, 0.05% at 143 GHz, 0.04% at 217 GHz, and negligible at 353 GHz. The delivered 100–217 GHz maps have been scaled by these gain changes. It should be noted that these numbers are uncertain at the 20–30% level, depending on a multitude of details, such as how the telescope is modelled.

For the planet photometry, some level of knowledge of the amplitude of the far sidelobes is needed to correctly compare the reconstructed flux with the planet brightness. However, the relative far sidelobe power is lower than 0.3% (Tauber et al. 2010) for all HFI frequencies, which is well below the systematic uncertainties of the planet emission models we are using, which are around 5% (see Sect. 3.4). Therefore far sidelobes can safely be ignored in the 545 and 857 GHz calibration.
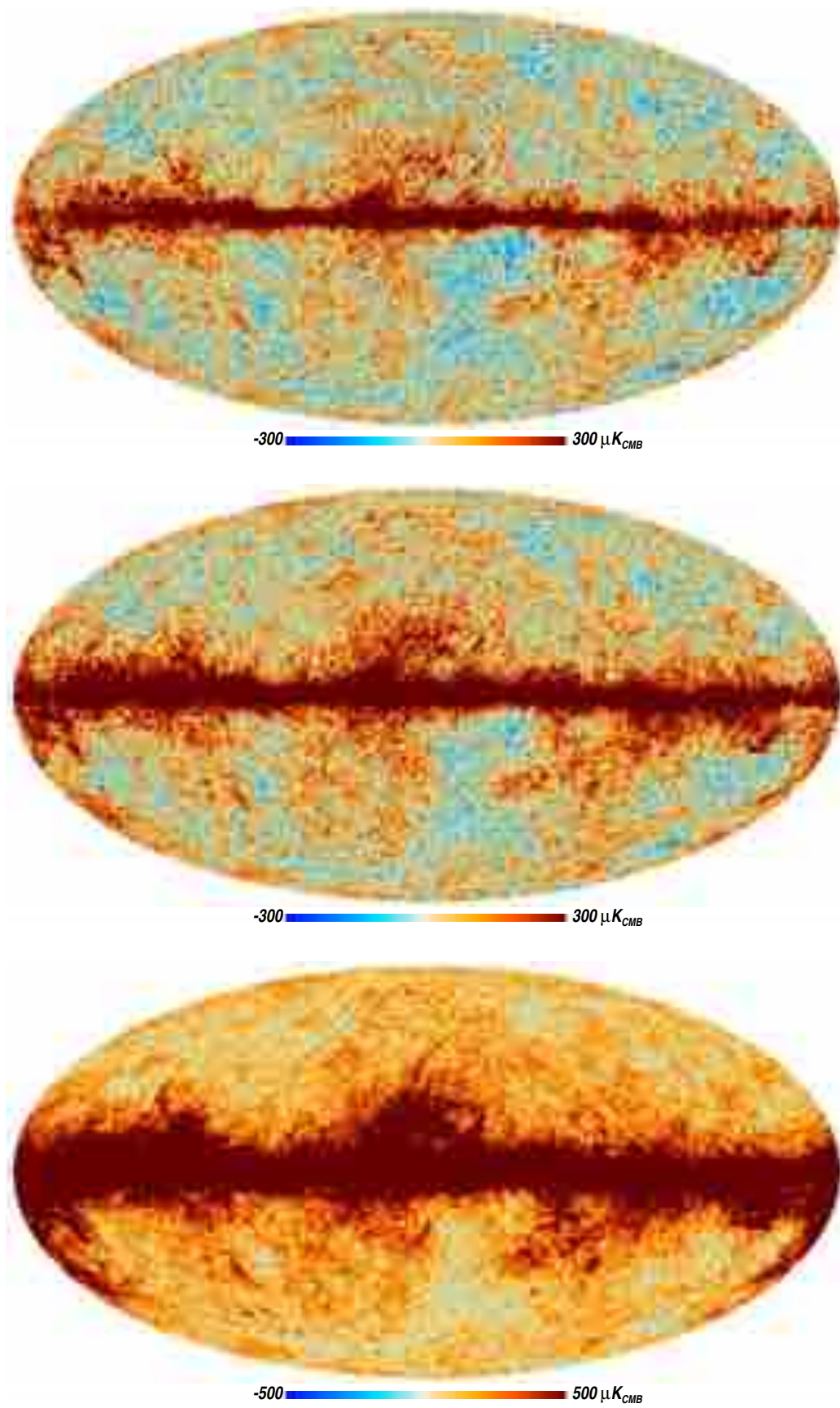
Fig. 5. *Planck*-HFI full mission channel intensity maps at 100, 143, and 217 GHz (*from top to bottom*) after removal of zodiacal emission.
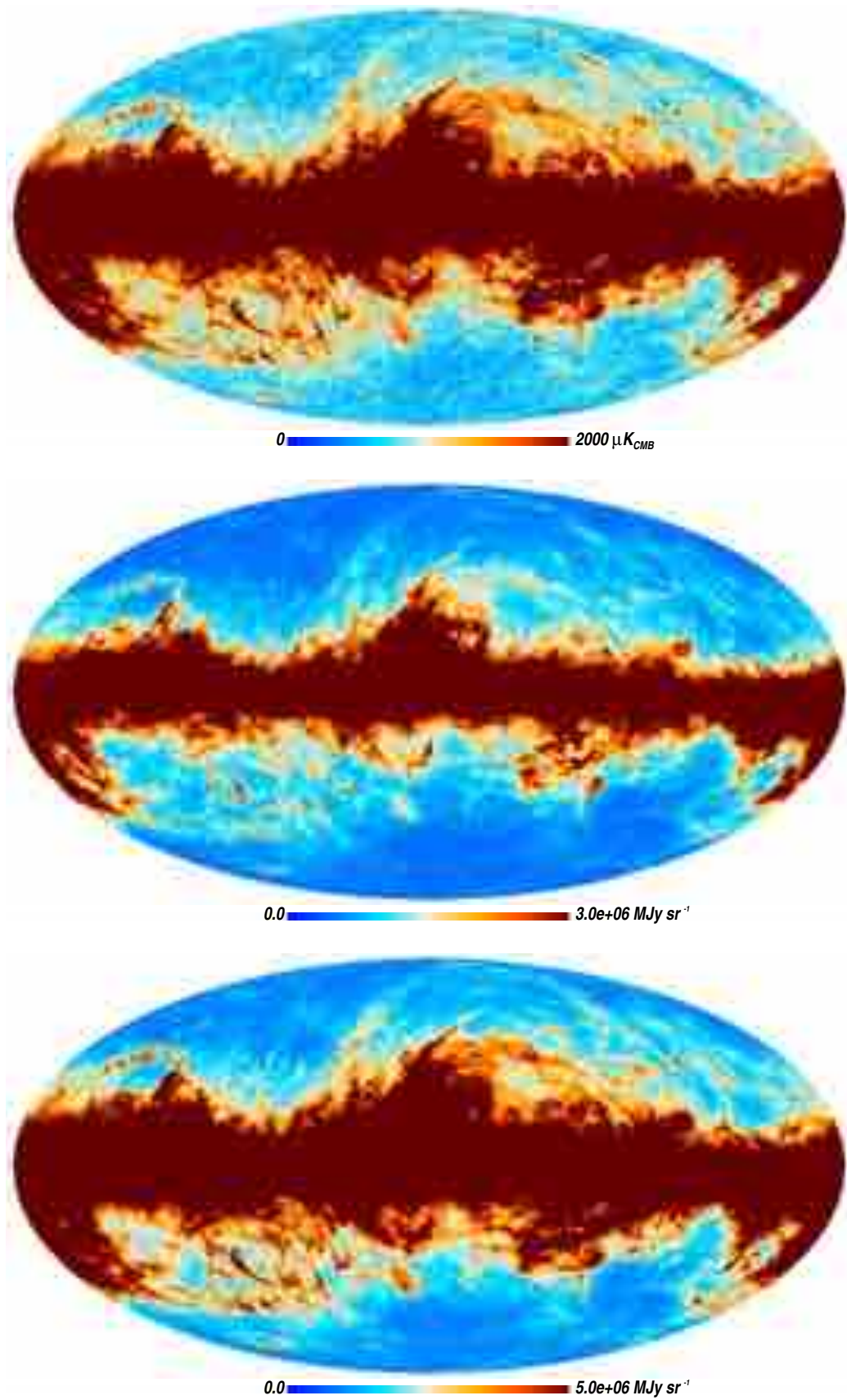
Fig. 6. *Planck*-HFI full mission channel intensity maps at 353, 545, and 857 GHz (*from top to bottom*) after removal of zodiacal emission.
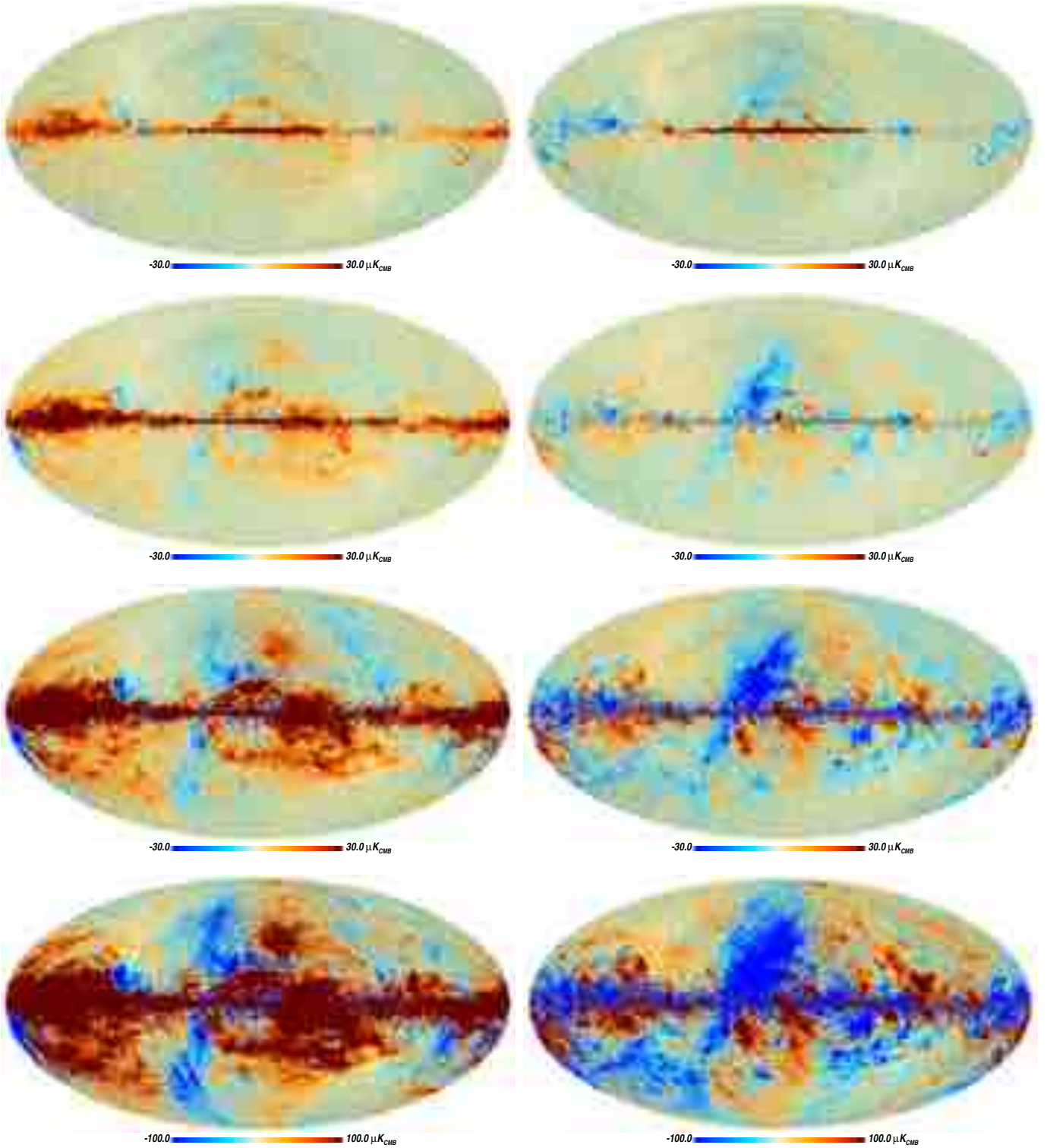
Fig. 7. *Planck*-HFI full mission *Q* (*left*) and *U* (*right*) polarization maps corrected from bandpass leakage (see Sect. 7.3.1). *from top to bottom*: 100 GHz, 143 GHz, 217 GHz, and 353 GHz.

5.4. Zodiacal emission

Zodiacal emission is reconstructed and subtracted in the same fashion as that used for the 2013 *Planck* results (Planck Collaboration XIV 2014). The basic procedure for characterizing and removing zodiacal emission from the *Planck* maps is to

– make frequency maps for each horn and survey as described in previous sections;

– make survey difference maps for each horn and year;

– find the date ranges over which each $N_{\mathrm{side}} = 256$ pixel was observed, and veto those pixels that were observed over a time-span of more than one week;

– use the COBE model (Kelsall et al. 1998) to recreate the different zodiacal emission components, assuming black-body emissivities;
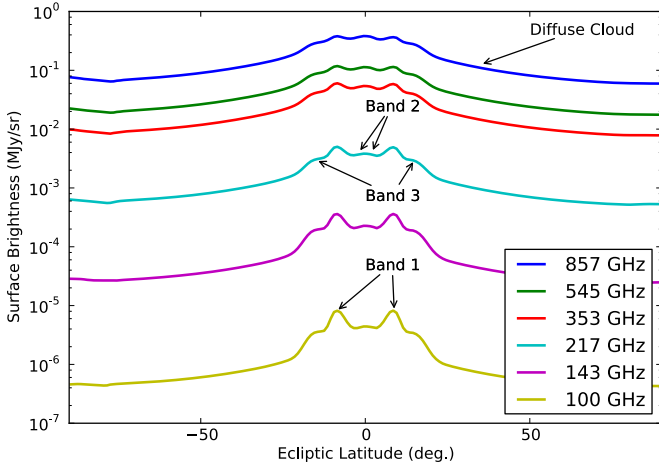
Fig. 8. Zodiacal light profiles for each HFI band (survey 3) binned in ecliptic latitude. The diffuse cloud and bands are each marked only once, but exist at the same latitudes at each frequency in differing relative amounts.

– fit the components to the survey difference maps for each horn and year to extract the actual emissivities;
– use the average of the fitted emissivities to reconstruct the implied zodiacal emission seen during each pointing period, for each horn, and remove these from each detector.

Figure 8 shows the profiles for each HFI band for survey 3, made by differencing maps made without zodiacal emission removal from those made with zodiacal emission removal and binning them in ecliptic latitude. The diffuse cloud and bands are each marked only once, but exist at the same latitudes at each frequency in differing relative amounts. These profiles also show some small offset effects near the ecliptic poles, which arise because the destriping is redone when zodiacal emission is removed.

The emissivities for each zodiacal component at each of the HFI frequencies are given in Table 3 and are plotted in Fig. 9. As noted in Planck Collaboration XIV (2014), there seems to be a jump between the emissivities for the bands at DIRBE wavelengths and the emissivities of Bands 1 and 3 at *Planck* wavelengths. This is being investigated, but is assumed to be a consequence of the assumption in the DIRBE analysis that all three bands have the same emissivities, while the *Planck* analysis allows them to be different. For the *Planck* cosmological studies this should be irrelevant, since the zodiacal analysis is being used only to remove the interplanetary dust contamination – the overall amplitudes of the emissivities, which are completely degenerate with the assumed particle density in the bands, are not being interpreted physically.

6. Noise description and subset differences

6.1. Map variance

As demonstrated in Paper A, the noise spectra for the *Planck*-HFI bolometers show significant deviation from white noise, resulting in correlations between pixels after map projection. At large scales, the correlations are dominated by low-frequency noise, while at high resolution neighbouring pixels are correlated as a result of time-response deconvolution and filtering. The *Planck* 2015 release does not provide a pixel-pixel correlation matrix; only the variance per pixel is given for each delivered
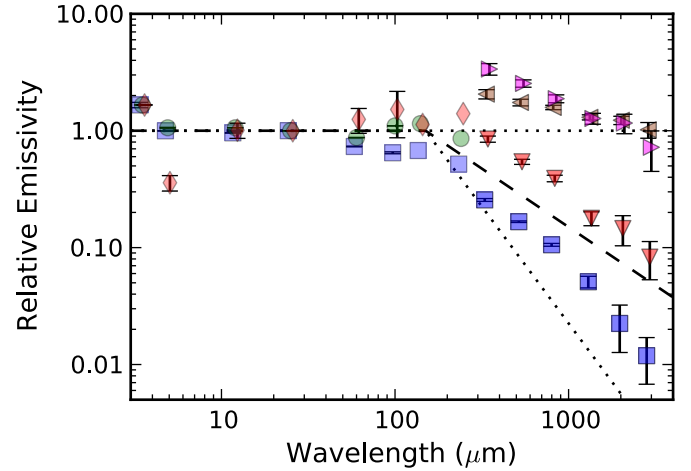

Fig. 9. Zodiacal emissivities. Data on the left, at wavelengths shorter than about 300 μm, are from COBE/DIRBE (Kelsall et al. 1998). Data for wavelengths greater than about 300 μm are from *Planck* (Table 3). In both cases, the blue squares represent the emissivity of the Diffuse Cloud. For DIRBE, the red diamonds represent the fitted emissivity for all three IRAS Bands, and the green circles show the values for the Circumsolar Ring and Trailing Blob. For *Planck*: the pink right-pointing triangles are for IRAS Band 3; the brown left-pointing triangles are for IRAS Band 1; and the red downward-pointing triangles are for IRAS Band 2. For reference, the lines show emissivities that are unity at wavelengths less than 250 μm, but proportional to λ^{-2}, λ^{-1}, and λ^0 at longer wavelengths.

Table 3. Frequency-averaged zodiacal emissivity values for the diffuse cloud and the three IRAS bands.

Frequency [GHz]	Cloud	Band 1	Band 2	Band 3
857	0.256 ± 0.007	2.06 ± 0.19	0.85 ± 0.05	3.37 ± 0.38
545	0.167 ± 0.002	1.74 ± 0.11	0.54 ± 0.03	2.54 ± 0.18
353	0.106 ± 0.003	1.58 ± 0.07	0.39 ± 0.02	1.88 ± 0.14
217	0.051 ± 0.006	1.30 ± 0.07	0.15 ± 0.02	1.27 ± 0.14
143	0.022 ± 0.010	1.23 ± 0.10	0.15 ± 0.04	1.16 ± 0.22
100	0.012 ± 0.005	1.02 ± 0.16	0.08 ± 0.03	0.72 ± 0.27

Notes. See also Fig. 9.

map. At first order, the variance maps are proportional to $1/N_{\rm hit}$, where $N_{\rm hit}$ is the number of samples per pixel.

The half-difference half-ring maps, projected using the same gain but destriped independently, are a good representation of the noise variance in the HFI maps. In the difference between the first and the second half of a ring, the sky signal vanishes almost completely. Moreover, most of the HFI systematics are scan-synchronous and thus also vanish in the difference.

Table 4 compares the noise per sample from three estimators: (a) the mean value of the pre-whitened variance map (i.e. scaled using the hit counts); (b) the variance of the pre-whitened half-ring half-difference map; and (c) the average of the half-ring map power spectra in the ℓ range 100–5000 (see Sect. 6.2). For polarization, the numbers are averages over Q and U for the maps and E and B for the spectra. The different estimators are sensitive to different kinds of systematic effects, such as time-response residuals and signal gradient in pixels. Nevertheless, the three noise estimators give very consistent results.

The variance maps (I–I, Q–Q, and U–U) are inhomogeneous owing to the *Planck* scanning (which have negligible
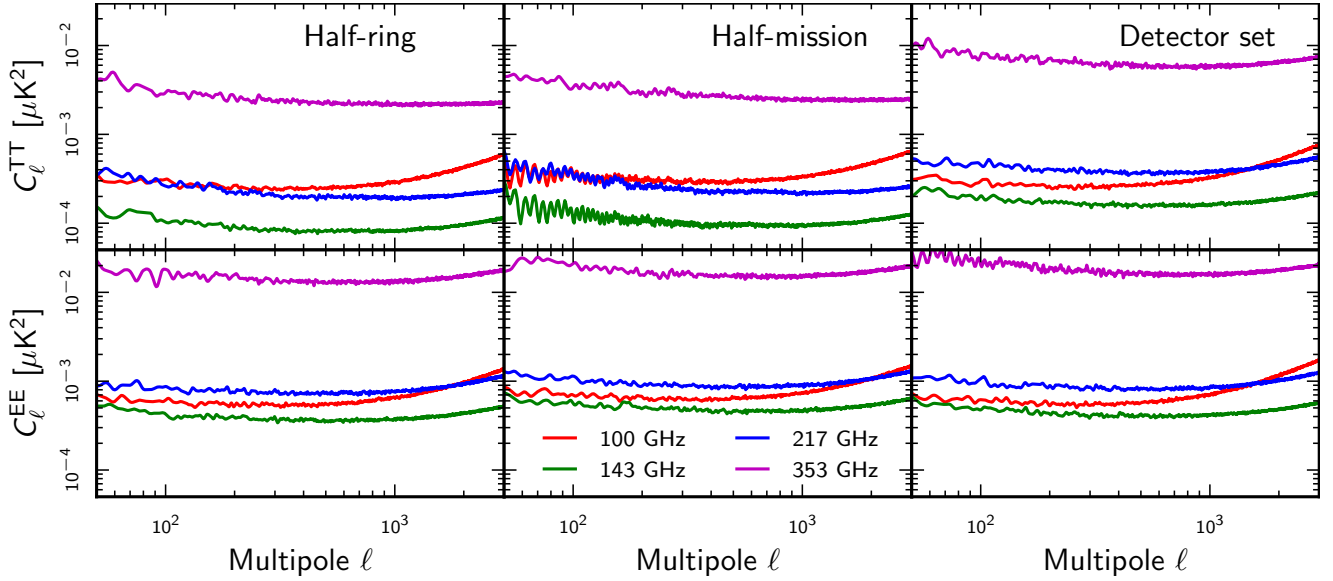
Fig. 10. *TT* and *EE* power spectra reconstructed from the half-difference between data subset maps for the dipole-calibrated channels.

Table 4. Estimation of the noise per sample for intensity (*I*) and polarization (*P*) estimated from (a) the variance maps; (b) the half-ring difference maps; and (c) the pseudo-spectra.

Frequency [GHz]	Variance maps (a)	Diff. maps (b)	Pseudo-spectra (c)
100I	1538	1531	1410
100P	2346	2344	2131
143I	769	758	759
143P	1631	1618	1611
217I	1105	1098	1141
217P	2512	2486	2440
353I	3692	3459	3780
353P	10 615	10 141	10 181
545I	0.612	0.619	0.779
857I	0.660	0.866	0.860

Notes. Units are μK_{CMB} for 100–353 GHz, and MJy sr^{-1} for the submm channels.

wobbling), the relative position of the detectors in the focal plane, and the rejection of some rings or groups of rings (see Paper A). Moreover, the typical HEALPix pixel size is about 1.′7 at $N_{side} = 2048$ resolution while *Planck* scans the sky on roughly (but not exactly) ecliptic meridians separated by 2.′5 (near the ecliptic equator). As a consequence, for single survey maps, lines of empty pixels appear between the scanning trajectories around $(l, b) = (0°, \pm 45°)$. Even when surveys are combined, inhomogeneities arise because the HEALPix pixels are elongated parallelograms. The axis of their elongation changes at the boundaries between the 12 primary HEALPix pixels. In the same regions of the sky and in Galactic coordinates, these elongations are parallel with the scanning trajectories, which induces moiré patterns in the coverage maps.

The degree of correlation between the Stokes parameters within each pixel reflects the distribution of the detector orientations, which results from the scanning strategy. The *I*–*Q* and *I*–*U* correlations are about 14, 9, 6, and 12% at 100, 143, 217, and 353 GHz. The *Q*–*U* correlation is about 11, 2, 3, and 8% at 100,143, 217, and 353 GHz. In Appendix A.2 we show the sky distribution of these correlations.

6.2. Map differences

The redundancy of the *Planck* scanning history and focal plane layout provides numerous ways to check data consistency. We can create differences between maps built using data splits, as described in Sect. 4.3. In the limit that the signal is the same in each data subset, the difference map should contain only noise. The TOI processing includes several operations that introduce correlations on various time scales; these are discussed below.

In the dipole-calibrated frequency channels (100–353 GHz), the signal differences are small enough that the data-split map differences can be evaluated at a spectral level, giving insight into the residual systematic errors. For high-frequency channels, we discuss the residuals in the map domain.

Given maps of two subsets of the data, M_A and M_B, we construct the half-difference as $\Delta M = (M_A - M_B)/2$. We compute the power spectrum in temperature and polarization of the half-difference, masking the sky with the *Planck* point source mask and the galaxy masks used in Planck Collaboration XI (2016), i.e. leaving 65, 59, 48, and 32% of the sky unmasked at 100, 143, 217, and 353 GHz, respectively.

In order to use this half-difference map to assess noise in the full maps, we account for widely varying integration time in the two subsets using a pixel-by-pixel weight map, which is multiplied by the half-difference map ΔM prior to computing the angular power spectrum. The weight is constructed as $W = 2/\sqrt{(1/n_A + 1/n_B)(n_A + n_B)}$, where n_A is the hit count map for M_A and n_B is the hit count map for M_B. In the limit that the half-difference map consists entirely of white noise, this exactly accounts for the differences in the hit counts. The *TT* and *EE* spectra of the difference maps are plotted in Fig. 10 and are described in the sections below. The *BB* spectra are nearly the same as the *EE* spectra and are not shown.

6.2.1. Half-ring map differences

The half-ring difference is sensitive to high-frequency noise, since most low-frequency modes (on time scales longer than 1 h) are common to both data sets and thus vanish. In the harmonic domain, the noise is nearly white with an amplitude compatible with the noise estimated in the map domain (see

Sect. 6.1). At large multipoles, the noise blows up because of the time transfer function deconvolution, before being cut off by the low-pass filter. At lower multipoles, half-ring differences show low-frequency noise residuals due to the destriping. Indeed, the destriping is performed independently for each half, or essentially half the data are used to solve the offsets for the full ring maps. The residuals from the offset determination are therefore expected to be twice as large as in the full-mission map.

In addition, the deglitching operation performed during the TOI processing uses the full data set to estimate the signal in each ring, thereby introducing some correlation between the two halves of each ring. Taking the difference between the two half-rings removes the correlated portion of the noise at the few percent level.

6.2.2. Half-mission map differences

With half-mission differences, we can check for long-time-scale variations and for apparent gain variation with time due to the analog-to-digital converter non-linearities. Moreover, because of the slightly shifted pointing between the first and second halves of the mission, the effect of a signal gradient within a pixel (especially on the Galactic plane where the signal is strong) is larger than for the half-ring map differences.

Because the number of observations in a given pixel can be very different between the two half-mission maps, using a weighting as described above is essential. Including the weighting, the half-mission differences give a power that is 10–20% higher than the corresponding half-ring difference. This fraction of additional power is nearly the same in all the channels 100–353 GHz, and is the same in both temperature and polarization. We understand this small additional power to be due to effects from the TOI processing that introduce correlations in the noise between the subsets. The half-ring maps, as stated above, have correlations introduced by the deglitcher that are subsequently removed by the differencing. These correlations are not present between the half-mission data sets, so their difference shows a higher noise power.

6.2.3. Detector-set map differences

This difference probes systematic effects that are bolometer-dependent. In the case of 143, 217, and 353 GHz, we note that the detector-set split excludes the unpolarized detectors, and the noise in TT is correspondingly higher than in the half-mission and half-ring split. The 100 GHz channel has only polarization-sensitive bolometers and the TT spectrum of the difference is much closer to the spectrum seen for the other data splits.

There are several other effects that make the power spectrum of the detector-set difference stand apart. A unique time response function is deconvolved from each bolometer. In the half-ring and half-mission data splits, the deconvolved function is identical in the two halves. With the detector-sets, however, the time response is in general slightly different in the two halves. This effect leads to a tilt in the spectrum of the detector-set difference maps relative to the half-ring or half-mission split. Moreover, at 353 GHz, signal residuals are larger owing to relative calibration uncertainties between detectors.

6.2.4. Map differences at low-ℓ

At low multipoles, despite the huge progress in the control of the systematics, data are still contaminated by systematic residuals.
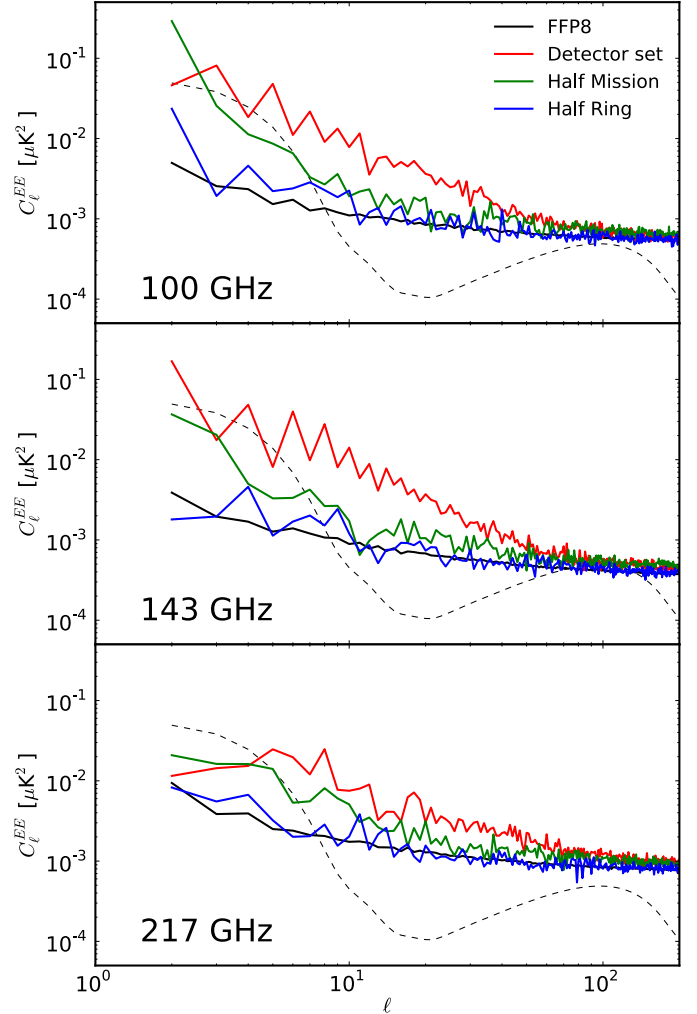

Fig. 11. *EE* power spectra reconstructed from the half-difference between data subset maps for the dipole-calibrated channels at low multipoles compared to the noise estimation from the FFP8 simulations. CMB signal from *Planck* 2015 is plotted in dashed lines.

Figure 11 shows the *EE* power spectra from the half-difference maps at 100, 143, and 217 GHz, and compared to the noise power spectrum from simulations (FFP8, described in Planck Collaboration XII (2016)). While the half-ring differences are compatible with noise, at multipoles typically lower than 50 the detector-set and half-mission differences are dominated by excess power that is larger than the *EE* CMB signal. The origin of the excess power will be explored in a forthcoming publication.

6.2.5. High-frequency channels

For the highest frequency channels (545 and 857 GHz) the data-split map differences are dominated by residual signals. Figure 12 shows the rms of the differences of intensity maps at 545 and 857 GHz for half-ring, half-mission, and year data splits compared to the same data split performed on a simulated noise map. At low signal, the difference is consistent with instrumental noise. At high signal levels, an additional residual appears in the difference map that is roughly proportional to the signal level. Part of this is due to pointing errors. For year and half-mission, the effect is enhanced by the combination of residual gain variations and the relative difference of pointing between the two splits. Over most of the sky, the signal is
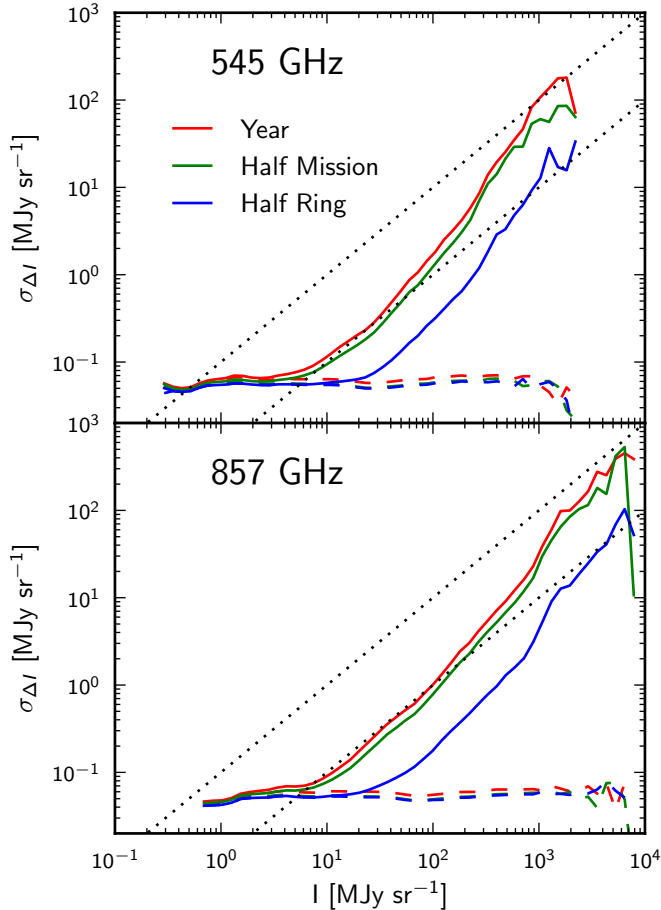
Fig. 12. Root mean square of the residual signal in difference maps at 545 and 857 GHz, as a function of signal level in the full map. The solid coloured curves show the rms of the data, while dashed coloured curves show the rms of a simulated noise map. The diagonal dotted lines indicate 1% and 10% of the signal.

reproducible to better than 1% for these frequencies. Bolometer map differences (not shown here) are, in addition, sensitive to the relative calibration error.

6.3. Noise cross-correlation

Here we check for correlations in the noise by computing cross-spectra between the difference maps described earlier. We look at 100 (Fig. 13), 143 (Fig. 14), and 217 GHz (Fig. 15) in comparison with the expectations from projecting noise realizations on the sky (using the FFP8 noise realizations described in Planck Collaboration XII (2016) and the end-to-end simulations described in Paper A).

When the half-mission cross-spectra of half-ring differences are computed, the results are roughly consistent with the FFP8 noise simulations. At 143 GHz in temperature, the end-to-end simulation produces a slight rise in power at low multipoles that is not seen in the data.

Large correlations are seen in the half-ring cross-spectra of half-mission differences. These are at least partially induced by our processing since the end-to-end simulations also show correlations that are not as large in amplitude as those seen in the data, but show a similar spectral shape. These correlations are mainly due to the deglitcher, as described above.

6.4. Temperature-polarization cross-variance

In absence of spatial correlations, noise correlations between temperature I and polarized Q and U modes vanish in the harmonic domain, thanks to the orthogonality of the spherical harmonic decomposition. Consequently the TE and TB auto-spectra are not biased by noise in the way that the TT, EE, and BB spectra are. In practice, transfer function deconvolution, filtering, and pixelization effects can produce spatial correlations at high multipoles, resulting in a noise bias that is observed in the TE and TB angular power spectra. In Fig. 16 we compare the auto and cross-spectra for the half-ring, half-mission, and detector set splits. These pseudo-spectra have been built by masking Galactic emission and point sources (approximately 40% of the sky). The auto-spectra are biased at high multipoles (starting at $\ell \approx 1500$). The amplitude of this bias and its sign depend on the frequency and on the mode considered. Nevertheless, none of the cross-spectra show significant departures from the null expectation.

We observe that the amplitude of the noise bias in auto-spectra is mitigated when adding more independent data sets, such as detectors or surveys (survey maps show larger amplitude than half-mission and full-mission). These results are fully reproduced in the FFP8 simulations.

6.5. Subset map cross-covariance

When mapping subsets of the available data (selecting detectors and/or time spans) we have a choice between solving for independent baseline offsets for the subset in question or reusing full-mission, full-frequency baselines (as in the 2015 HFI map release). Full-mission baselines are more accurate, leaving less large-scale noise in the maps, but introduce noise correlation between detector-set maps.

We can measure the resulting bias in cross-spectra through noise simulations. Comparison between noise spectra from a Monte Carlo analysis at 100 GHz using both methods of de-striping is shown in Fig. 17 for the case of detector sets. Noise spectra for each detector set show more large-scale power when using independent baselines than in the full mission case. On the other hand, the cross-power spectrum is biased by up to a few times 10^{-3} μK^2 below $\ell = 10$; the same is true for the half-mission subset.

7. Systematic effects

We now describe the major systematic effects that could potentially affect the maps: the gain variations; errors in the absolute gain determination; errors in the polarization efficiency and orientation; and, most of all, the detector-to-detector gain mismatch. The latter includes bandpass mismatch (which affects the response to the foregrounds of the detectors at the same frequency) and relative gain uncertainties, both of which create intensity-to-polarization leakage. All these effects are constrained using tests involving the combination of maps, residuals in maps, cross-power spectra, and dedicated simulations.

7.1. Gain stability

Gain stability has been significantly improved with respect to the *Planck* 2013 release. This is mainly due to the analog-to-digital converter non-linearity correction, combined with the new determination of the time transfer function (see Paper A). The amplitude of the apparent gain variation has been improved
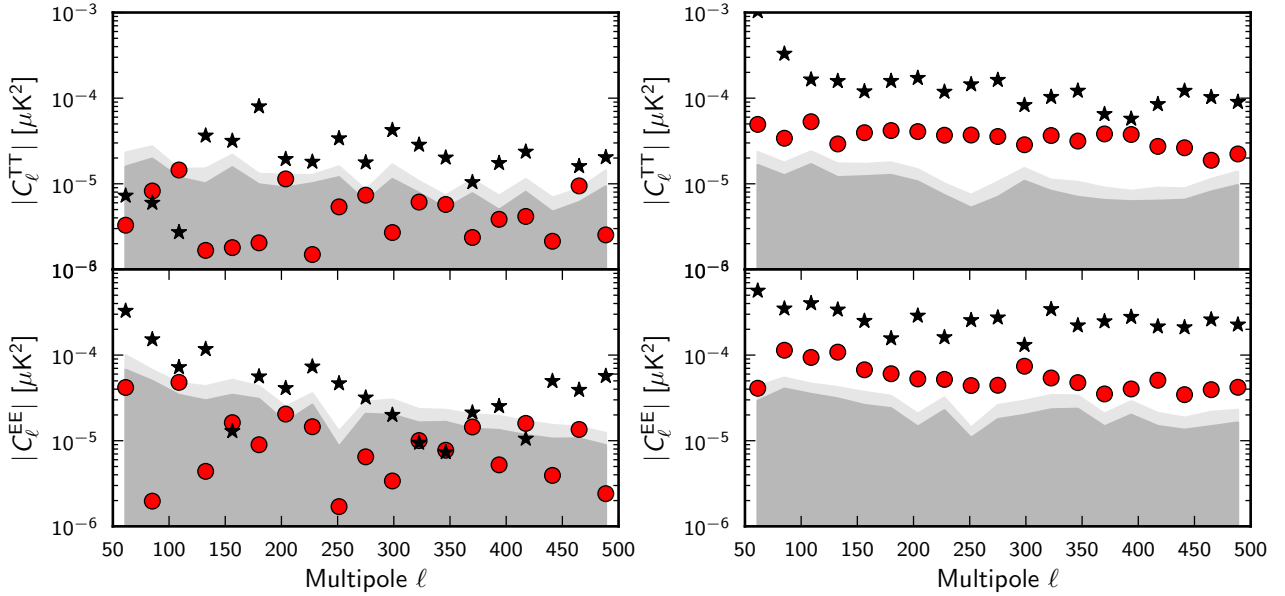
Fig. 13. 100 GHz difference map cross spectra. *Left*: half-mission (HM) correlation of half-ring differences (HR). *Right*: half-ring (HR) correlation of half-mission difference (HM). The real data are red dots. The end-to-end simulation are black stars. One and two sigma contours from ten FFP8 noise realizations are shaded grey.
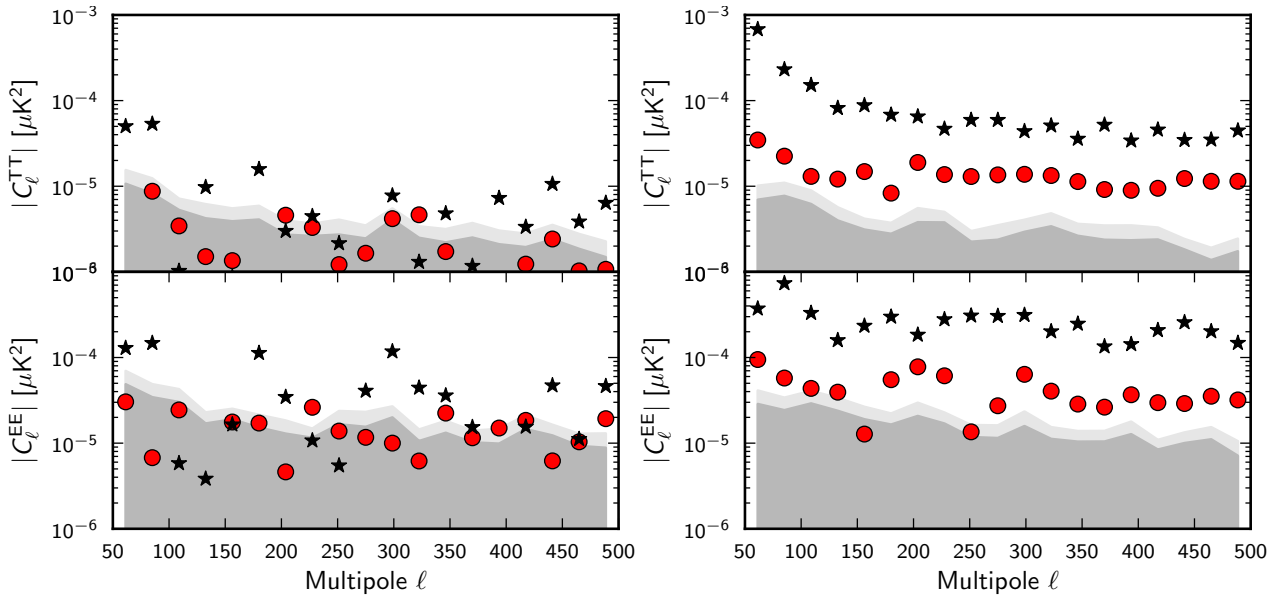

Fig. 14. Same as Fig. 13 for 143 GHz difference map cross spectra.

from 1–2% to less than 0.5% for all cases. Residual gain variations are compatible with zero when including the correction for the long-time-constant residuals, as discussed in Sect. 3.3.

We check the stability of the gain over time using the same tool as in Planck Collaboration VIII (2014) called `bogopix`. For each bolometer, the code fits simultaneously for the gain g_r and the offsets o_r for each ring, marginalizing over the sky signal T:

$$P_t = g_r \times (A_{tp} \cdot T_p + t_{\mathrm{orb}}) + o_r + n_t. \tag{15}$$

Given the low amplitude of the observed gain variations (less than 0.5%), we linearize Eq. (15) and solve by iteration (see Planck Collaboration VIII 2014); one or two iterations are sufficient to ensure convergence. To initialize the iterations, we start from the constant gain solution G (see Sect. 3.2).

We compute the gain variations from single-bolometer data (neglecting polarization). Polarized signals will affect the gain determination. To reduce this bias, we ignore sky regions where the polarized emission is the strongest, which lie mostly in the Galactic plane.

Figure 18 shows the results of `bogopix` for bolometers at 100, 143, and 217 GHz, smoothed over a four-day period. At higher frequencies (353 GHz and above), the gain variations are much lower than the gain uncertainty. Owing to the *Planck* scanning strategy, the Galactic foreground is larger for some rings, while the orbital dipole amplitude is almost constant. This increases the dispersion around those regions and potentially induces some bias in the gain determination. In the end, we find gain variations with amplitudes lower than 0.3, 0.4, and 0.5% at 100, 143, and 217 GHz, respectively.
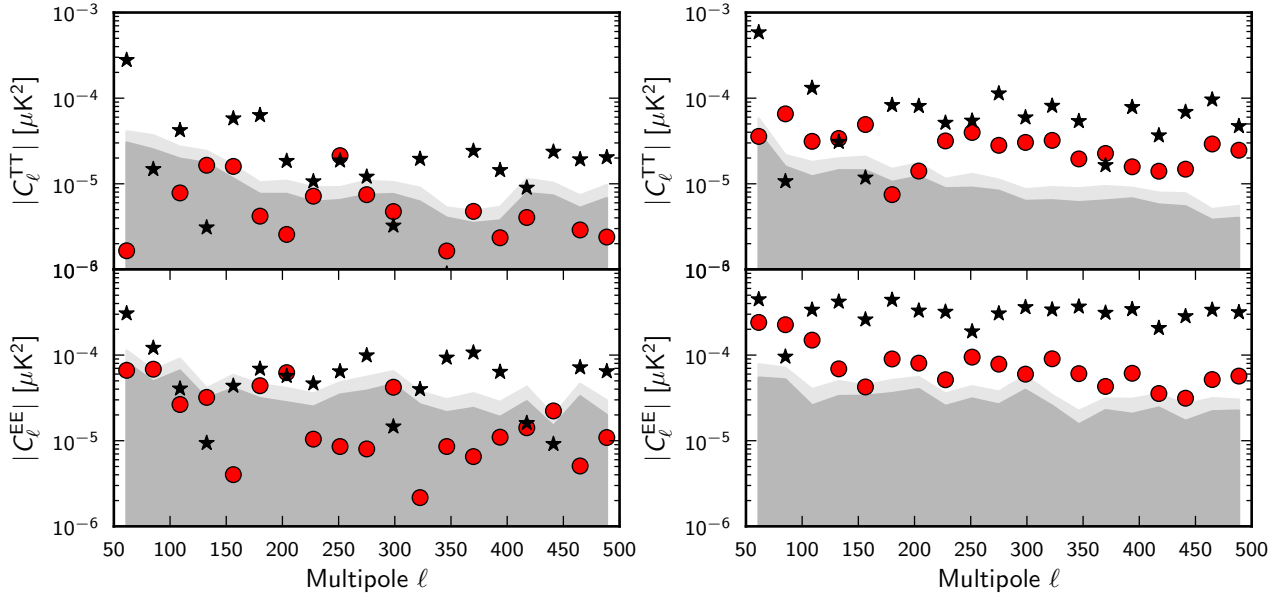
Fig. 15. Same as Fig. 13 for 217 GHz difference map cross spectra.

The residual apparent gain variations are essentially coming from the uncertainty in the current analog-to-digital converter non-linearity correction, the uncertainty in the long-time-constant estimation, and the effect of long-term thermal variations on the bolometer and electronics response.

7.2. Calibration accuracy

7.2.1. Inter-frequency accuracy

The precision of the calibration can be assessed by looking for residual dipoles in the maps. If the calibration of a map is slightly incorrect, the removal of the solar dipole in the mapmaking process leaves a residual dipole. However, identifying such a residual dipole is difficult because of the presence of other sources of power at $\ell = 1$, mostly due to Galactic emission and zodiacal light, but also to imperfect correction of systematic effects such as far sidelobes.

Following the method presented in Sect. 5.1 used to estimate the solar dipole direction and amplitude, we cleaned the Galactic emission from the HFI maps using a local correlation with the 857 GHz map. Adding the solar dipole that was removed in the mapmaking process (Sect. 5.1) to $D_{\rm res}$ produces a map that contains the true solar dipole. We then fit for its amplitude, fixing its direction to the official *Planck* value (lon, lat = 264°.00, 48°.24) to limit the effect of other residuals still present in $D_{\rm res}$ (Galactic, systematic effects). The fit is done using sky pixels where $I_{857} <$ 2 (faintest 37% of the sky) to limit the effect of Galactic emission residuals (CO, free-free emission, and small scale dust spectral energy distribution variations). Table 5 gives the ratio of fitted amplitude to the removed dipole found for the HFI maps at frequencies from 100 to 545 GHz. Because effects other than a miscalibration can contribute to a residual dipole in the maps, these ratios provide upper limits on the calibration accuracy at each frequency. The results indicate that the calibration at 100 and 143 GHz is precise at a level of few 10^{-4}. At 217 GHz, the fit is compatible with a residual dipole at the 0.2% level. At higher frequencies, the fits indicates residuals at 0.52% and 1.23% at 353 and 545 GHz, respectively.

These results are in agreement with those obtained while performing component separation, as shown in Table 4 from

Table 5. Ratio of amplitudes of the fitted dipole ($A_{\rm fit}$) and the removed dipole ($A_{\rm rm} = 3364.5\,\mu$K).

Frequency [GHz]	$A_{\rm fit}/A_{\rm rm}$	Statitiscal uncertainties	Systematic uncertainties
100	1.00010	±0.00006	±0.0001
143	0.99988	±0.00012	±0.0001
217	1.00184	±0.00027	±0.0003
353	1.00568	±0.00185	±0.0020
545	1.02515	±0.01627	±0.0190

Notes. The direction of the dipole removed from the data (lon = 264°.00, lat = 48°.24) was constrained here. The fit was computed for different sky fractions from 30 to 70%. Statistical and systematic uncertainties are also indicated.

Planck Collaboration IX (2016) and in Planck Collaboration X (2016). They are also in agreement with the results from the cosmological parameter determination, where intercalibration coefficients are also fitted for (see Planck Collaboration XI 2016). The agreement between these measurements computed over different multipole ranges highlights the quality of the *Planck*-HFI calibration, together with the accuracy of the transfer function reconstruction.

7.2.2. Intra-frequency accuracy

For polarization reconstruction with *Planck*-HFI data, we have to combine data from several detectors. Any relative calibration error will induce an intensity-to-polarization leakage (see Sect. 7.3). For the CMB channels, we have assessed the relative calibration accuracy for each detector at a given frequency using two complementary methods.

As in Sect. 6.2 (Fig. 14) of Planck Collaboration VIII (2014), we derive relative inter-calibration factors for each detector (for 100 to 353 GHz), rescaling their cross-pseudo-power spectra, estimated over 40% of the sky (30% for 353 GHz) in the ℓ range 25–300, which encompasses the first acoustic peak. We used colour-correction factors at 353 GHz, because even at high latitude the dust emission is large. As in 2013,
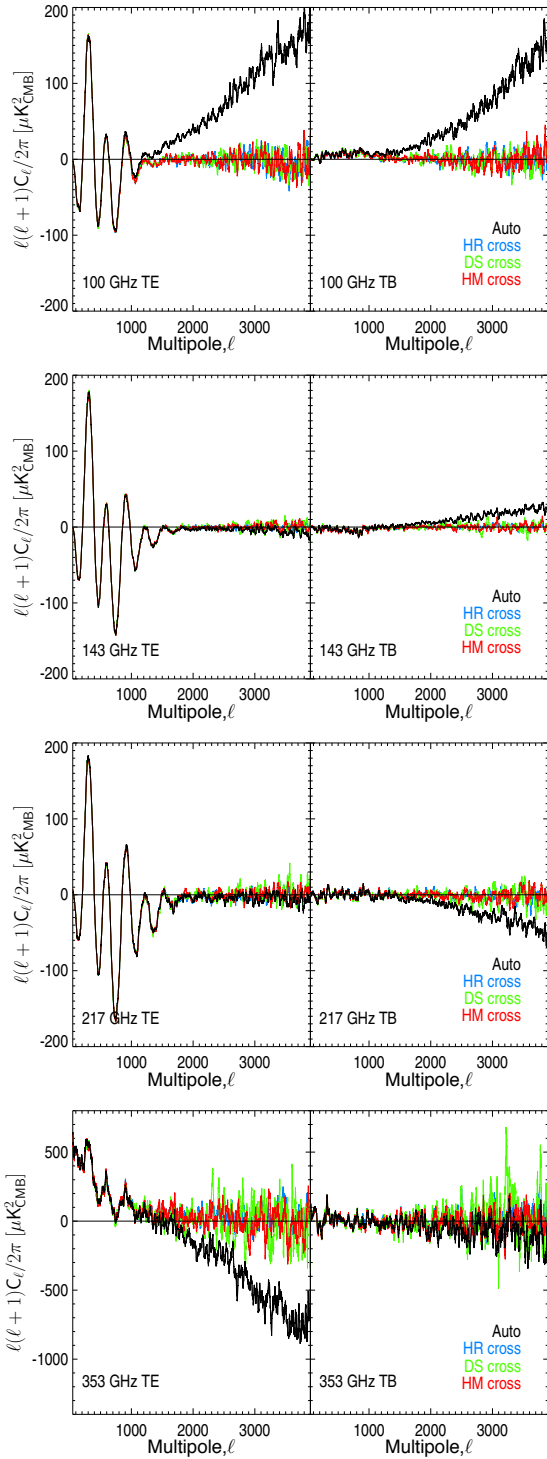
Fig. 17. Average *EE* spectra obtained from 100 simulations of detector-set noise maps. The maps were produced using either the full-mission baseline destriping (MBD) or the destriping run on each subset independently (run baseline destriping or RBD). Both the increased low-ℓ noise in the RBD case and the increased cross-spectrum noise bias in the MBD case are apparent.

Fig. 16. Pseudo-power spectra for *TE* (*left*) and *TB* (*right*) for each frequency (*from top to bottom*: 100, 143, 217, and 353 GHz). The auto-spectra are shown in black. Cross-spectra of half-ring (HR), half-mission (HM), and detector-set (DS) half-differences are shown in blue, red, and green, respectively. A Galaxy and point source mask, leaving 40% of the sky, was used in all cases.

we keep the maximum of these factors as a conservative estimate of the relative calibration accuracy. In 2015, we find 0.09, 0.07, 0.16, and 0.78% for 100, 143, 217, and 353 GHz, respectively (compared to 0.39, 0.28, 0.21, and 1.35% in 2013). Since single-detector maps are built ignoring polarization, these values
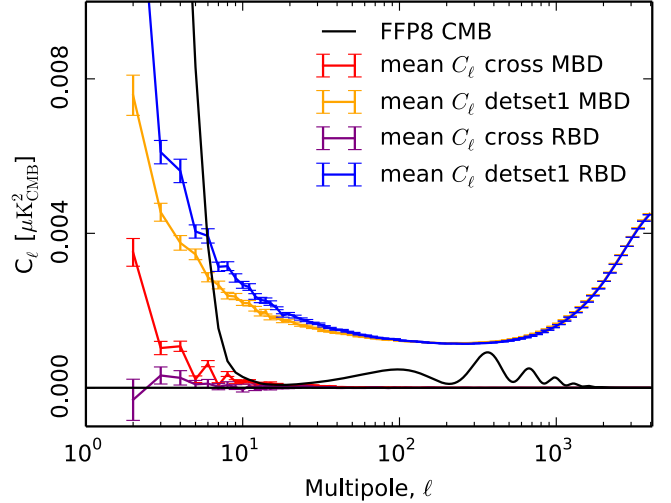
should be considered as conservative upper limits on the relative detector-to-detector calibration accuracy.

We complemented these estimations by analysing the solar dipole residual on the differences of single detector maps. We fit the dipole amplitude fixing its direction while masking 30% of the sky in the Galactic plane to avoid regions affected by band-pass differences. We find maximum amplitudes 0.5, 0.6, and 3.0 μK for 100, 143, and 217 GHz, respectively, which – relative to the solar dipole amplitude (3364.5 μK, see Sect. 5.1) – gives accuracies of the same order as the aforementioned spectra analysis. As in this previous method, the main limitation comes from polarization which is ignored in the single detector maps.

While significantly better than for the 2013 release, calibration mismatch between bolometers at a given frequency is one of the main systematic residuals contaminating the HFI large angular scales in polarization, as explained in the next section.

7.3. Intensity-to-polarization leakage

Any gain mismatch between the measurements of detectors belonging to the same frequency channel will result in intensity-to-polarization and cross-polarization leakage in the channel maps. In *Planck*, the dominant leakage effect has three main origins:

- monopole mismatch from the uncertainty in the mean offset determination;
- gain mismatch that produces leakage from the whole intensity signal into polarization;
- bandpass mismatch that mainly generates intensity-to-polarization leakage from foreground emission (with a non-CMB spectrum). In the case of HFI, the leakage effect is dominated by CO and thermal dust emission.

All these leakage sources are especially important for the large angular scales. Beam-mismatch polarization leakage occurs at small angular scales and is discussed in Paper A. Although the first two mismatches can be minimized by obtaining more accurate measurements of offsets and gains, respectively, the
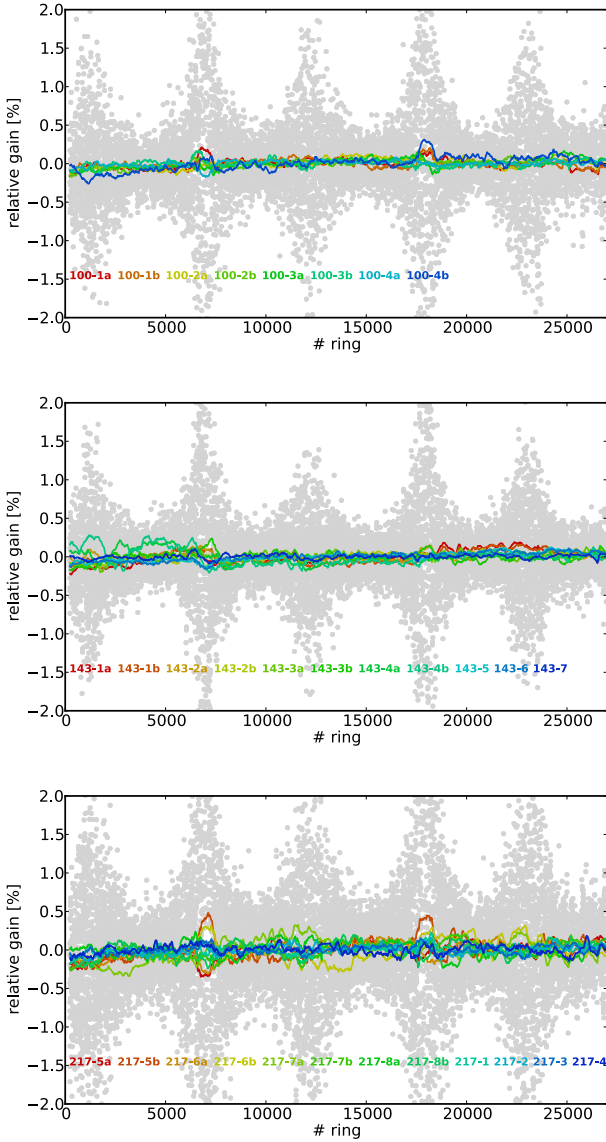
Fig. 18. Gain variation with ring number for each bolometer estimated using `bogopix`. *From top to bottom:* 100, 143, and 217 GHz. Gain values for individual rings (grey dots) have been smoothed with a four-day width. The gain variations are lower than 0.3, 0.4, and 0.5% at 100, 143, and 217 GHz, respectively.

bandpass mismatch cannot be removed in the mapmaking process if we want to project CMB and foregrounds at the same time.

The power absorbed by a given bolometer b at time t is expressed using the Stokes parameters (I_p, Q_p, U_p), which characterize the emission in intensity and polarization in the corresponding sky pixel p. The polarized HFI channels are calibrated using the CMB orbital dipole and the total calibrated power absorbed by the bolometer b can be written as

$$m_t^b = (1 + \epsilon_{\text{gain}}^b)$$
$$\times \left\{ \sum_k C_k (1 + \epsilon_{\text{BP},k}^b) \left[I_p^k + \rho^b \left(Q_p^k \cos \phi_t^b + U_p^k \sin \phi_t^b \right) \right] \right\}$$
$$+ \epsilon_{\text{offset}}^b + n_t, \tag{16}$$

where the polarization efficiency ρ^b and the polarization angle $\phi_t^b = 2(\psi_t + \alpha^b)$ are explicitly dependent on the bolometer b,

with the index k ranging over the different sky components. Additionally, we have the following definitions:

- ϵ_{gain}^b encodes the gain mismatch of bolometer b with respect to the mean calibration of the channel;
- $\epsilon_{\text{offset}}^b$ corresponds to the overall offset of bolometer b, which is small but not vanishing;
- $\epsilon_{\text{BP},k}^b$ is the bandpass mismatch specific to bolometer b, which affects all sky components except the CMB (see description below);
- C_k is the average transmission of sky component k in a given channel.

Each of these ϵ terms is responsible for leakage from intensity to polarization in a manner that can in principle be quantified and corrected for, as described hereafter. We note that we only consider first-order terms in ϵ, as any higher-order contribution is negligible.

7.3.1. Bandpass mismatch

Each emission component k (where k = CMB, dust, synchrotron, etc.) is integrated over the bandpass of the detector according to a given spectrum $f_k(\nu)$. Since the polarized HFI channels are calibrated using the CMB orbital dipole, we define the transmission coefficients

$$C_k^b = \frac{\int f_k(\nu) H_\nu^b \, d\nu}{\int f_{\text{CMB}}(\nu) H_\nu^b \, d\nu} \tag{17}$$
$$\equiv C_k \left(1 + \epsilon_{\text{BP},k}^b \right),$$

where H_ν^b is the spectral response of bolometer b and $C_k = \sum_b C_k^b / N_{\text{bolo}}$ is the average value of the C_k^b in a given channel. These transmission coefficients express the k-component emission in CMB units. If all bolometers had the same spectral responses then $\epsilon_{\text{BP},k}^b$ would be equal to zero, i.e. $C_k^b = C_k$, in which case no leakage related to bandpass-mismatch would be produced.

Considering only bandpass mismatch corresponds to setting $\epsilon_{\text{gain}}^b = 0$ and $\epsilon_{\text{offset}}^b = 0$ in Eq. (16). Then, ordering all the data samples, m_t^b, for a bolometer observing a position p on the sky into a single vector $\boldsymbol{D}^b$, defining A to be the pointing matrix in temperature and polarization, and n the noise vector, Eq. (16) reads

$$\boldsymbol{D}^b = \sum_k C_k \mathsf{A} \begin{pmatrix} I_p^k \\ Q_p^k \\ U_p^k \end{pmatrix} + \sum_k C_k \epsilon_{\text{BP},k}^b \mathsf{A} \begin{pmatrix} I_p^k \\ Q_p^k \\ U_p^k \end{pmatrix} + \boldsymbol{n}. \tag{18}$$

Using all bolometers b within a channel, the mapmaking procedure solves for the total signal Stokes parameters $(I_p^{\text{tot}}, Q_p^{\text{tot}}, U_p^{\text{tot}})$ in pixel p, formally computing,

$$\begin{pmatrix} I_p^{\text{tot}} \\ Q_p^{\text{tot}} \\ U_p^{\text{tot}} \end{pmatrix} = \left(\mathsf{A}^T \mathsf{N}^{-1} \mathsf{A} \right)^{-1} \mathsf{A}^T \mathsf{N}^{-1} \boldsymbol{D}, \tag{19}$$

which becomes

$$\begin{pmatrix} I_p^{\text{tot}} \\ Q_p^{\text{tot}} \\ U_p^{\text{tot}} \end{pmatrix} = \sum_k C_k \begin{pmatrix} I_p^k \\ Q_p^k \\ U_p^k \end{pmatrix} + \sum_k C_k \sum_{b=0}^{N_b - 1} \epsilon_{\text{BP},k}^b \Gamma_p^b \begin{pmatrix} I_p^k \\ Q_p^k \\ U_p^k \end{pmatrix}, \tag{20}$$

where $\Gamma_p^b \equiv \left(\mathsf{A}^T \mathsf{N}^{-1} \mathsf{A} \right)^{-1} \mathsf{A}^T \mathsf{N}^{-1} \Delta^b \mathsf{A}$. We have introduced the matrix Δ^b, the elements of which are equal to zero except for the diagonal elements relevant to bolometer b, which are set to 1. The

last term of Eq. (20) is the leakage term in pixel p, where intensity will leak into Q and U, Q into I and U, and U into I and Q, according to the mismatch coefficients $\epsilon^b_{\mathrm{BP},k}$ and the values of the 3×3 matrix

$$\Gamma^b_p = \begin{pmatrix} \Gamma_{II} & \Gamma_{QI} & \Gamma_{UI} \\ \Gamma_{IQ} & \Gamma_{QQ} & \Gamma_{UQ} \\ \Gamma_{IU} & \Gamma_{QU} & \Gamma_{UU} \end{pmatrix}^b_p . \tag{21}$$

Considering all pixels, the quantities Γ^b_{XX} correspond to nine sky maps for bolometer b. These maps can be fully determined from the mapmaking solution and may be understood as patterns of the mismatch leakage. In practice, cross-polarization leakage and polarization-to-intensity leakage are negligible compared to the intensity-to-polarization contribution and we therefore consider the latter only. The Γ_{IQ} and Γ_{IU} maps have been systematically produced by the mapmaking pipeline[4]. With these assumptions, the leakage induced by bandpass-mismatch in Q and U for the sky component k reads

$$L^{\mathrm{BP},k}_{IQ,IU} = C_k I^k \sum_{b=0}^{N_{\mathrm{bolo}}-1} \epsilon^b_{\mathrm{BP},k} \Gamma^b_{IQ,IU}. \tag{22}$$

In consequence, for a given calibrated intensity template of the sky component k (i.e. $I^k_{\mathrm{template}} = C_k I^k$) we can compute leakage correction maps as

$$L^{\mathrm{corr},k}_{IQ,IU} = I^k_{\mathrm{template}} \sum_{b=0}^{N_{\mathrm{bolo}}-1} \epsilon^b_{\mathrm{BP},k} \Gamma^b_{IQ,IU} = I^k_{\mathrm{template}} \sum_{b=0}^{N_{\mathrm{bolo}}-1} \frac{C^b_k}{C_k} \Gamma^b_{IQ,IU}, \tag{23}$$

where the last equality assumes $\sum_{b=0}^{N_{\mathrm{bolo}}-1} \Gamma^b_{IQ,IU} = 0$ by construction.

Leakage correction maps have been produced for all polarized HFI channels. The relevant foregrounds at these frequencies are dust (all channels) and CO (all channels except 143 GHz). To do so, the coefficients C^b_{dust} have been computed from Eq. (17), where the spectral responses of the bolometers $H^b(\nu)$ are those obtained from pre-launch ground-based measurements of the bandpasses (Planck Collaboration IX 2014). The dust spectrum is taken as a grey body with spectral index $\beta = 1.62$ and temperature $T = 19.7$ K, which are the all-sky average values found in Planck Collaboration XI (2014). For the intensity template required in Eq. (23), we use the thermal dust intensity maps at 353 GHz obtained from the *Planck* thermal dust model (Planck Collaboration XI 2014). Combining all these ingredients, the dust correction maps $L^{\mathrm{corr\,(dust)}}_{IQ,IU}$ are produced according to Eq. (23) and delivered in the 2015 HFI data release (Fig. 19).

We note, however, that the reliability of these corrections is limited by uncertainties both in the physical nature of the foreground components and in the determination of the bolometer spectral responses. For the sake of simplicity, a constant spectral index and a constant temperature across the sky have been assumed for the thermal dust emission. Furthermore, the calibrated thermal dust intensity templates are those derived from the 2013 *Planck* thermal dust model; although they are close, these templates do not strictly correspond to the calibration of the 2015 maps. Also, the leakage corrections are particularly sensitive to the differences in transmission between bolometers (i.e. the C^b_k coefficients); small uncertainties on those will

---

[4] The Γ_{II} pattern map quantifies the correction that should, in principle, be brought to the I channel map, given that some intensity has leaked into polarization. The correction is, however, negligible and is not taken into account here. The same is true for Γ_{QQ} and Γ_{UU}.
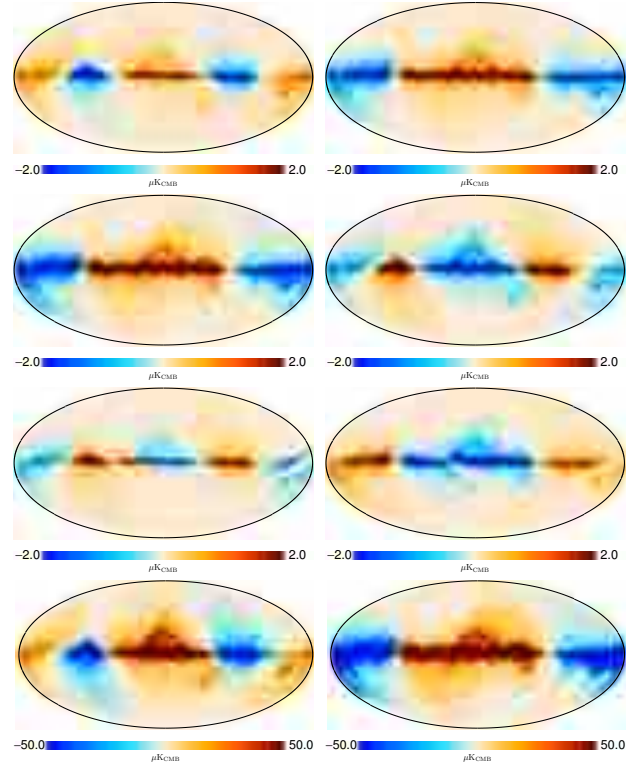
Fig. 19. Dust leakage correction maps from ground-based measurements of the bandpass in Q (*left*) and U (*right*) at all HFI channels: 100, 143, 217, and 353 GHz (*from top to bottom*).

yield large uncertainties in the final correction maps. In conclusion, the bandpass leakage corrections should not be taken at face value, but should be thought of as order-of-magnitude estimates only. We only advocate the use of these correction maps to test the stability and estimate uncertainties of any further results using the HFI polarization maps. A result solely obtained by applying the corrections will not be reliable.

7.3.2. Calibration and monopole mismatches

Using the same formalism as above, calibration mismatch is computed by setting $\epsilon^b_{\mathrm{BP},k} = 0$ and $\epsilon^b_{\mathrm{offset}} = 0$ in Eq. (16). Following closely Sect. 7.3.1, one finds that the total intensity-to-polarization leakage due to calibration mismatch is

$$L^{\mathrm{gain}}_{IQ,IU} = \sum_k C_k I^k \times \sum_{b=0}^{N_{\mathrm{bolo}}-1} \epsilon^b_{\mathrm{gain}} \Gamma^b_{IQ,IU}$$
$$\approx I^{\mathrm{dipole}} \times \sum_{b=0}^{N_{\mathrm{bolo}}-1} \epsilon^b_{\mathrm{gain}} \Gamma^b_{IQ,IU}, \tag{24}$$

where at first order, for low-frequency maps, the solar dipole signal ($k = $ dipole, $C_{\mathrm{dipole}} = 1$ by construction) provides the dominant contribution to the calibration mismatch leakage effect.

Setting $\epsilon^b_{\mathrm{BP},k} = 0$ and $\epsilon^b_{\mathrm{gain}} = 0$ in Eq. (16), one shows in a similar fashion that the monopole intensity-to-polarization leakage is simply

$$L^{\mathrm{mono}}_{IQ,IU} = \sum_{b=0}^{N_{\mathrm{bolo}}-1} \epsilon^b_{\mathrm{offset}} \Gamma^b_{IQ,IU}, \tag{25}$$

where the monopole mismatch is modelled using a constant sky template $I^{\text{monopole}} = 1$, while the amplitude of the mismatch is encoded in $\epsilon_{\text{offset}}^b$.

Although the bandpass mismatch coefficients $\epsilon_{\text{BP,dust}}^b$ can be evaluated directly from foreground modelling (assuming a given spectrum of the dust and using the spectral responses of the detectors), this is not the case for ϵ_{gain}^b and $\epsilon_{\text{offset}}^b$. It is therefore not possible to provide correction maps for these leakage effects by computing Eqs. (24) and (25) directly. However, one can consider the possibility of fitting these quantities from the maps themselves by using the $I^{\text{dipole}} \times \Gamma_{IQ,IU}^b$ and $\Gamma_{IQ,IU}^b$ as templates of the gain and monopole leakages, respectively. Such a method, known as the generalized global fit (GGF), has been implemented and is further described in Appendix A.3.2. The leakage maps produced with this method for the 353 GHz channel are delivered in the 2015 release and have been corrected simultaneously for leakages induced by bandpass, calibration, and monopole mismatches.

7.4. In-flight validation of the polarimeter efficiency and orientation

As discussed in Sect. 4.5, the polarimeter efficiency and orientation used in this release are taken from ground measurements (Rosset et al. 2010). In order to validate these numbers in flight, we used the Crab nebula maps obtained with the IRAM 30 m telescope and the 90 GHz XPOL polarimeter (Aumont et al. 2010). These maps consist of I, Q, and U measurements with an angular resolution of 27″ of a 10′-wide region around the Crab nebula (Tau A, M1, or NGC 1952, at J2000 coordinates RA = $5^h34^m32^s$ and Dec = $22°00′52″$). The same region was observed by *Planck* once per survey, with different scan directions for odd and even surveys. We compared single survey, single bolometer maps of the Crab region with a model obtained from the IRAM maps, and solved for the best values of polarimeter angle and efficiency.

From single survey, single bolometer data we can only solve for an intensity map, which projects on the sky the total power P_t described in Eq. (1). This power depends on the true value of the polarization angle α specific to the detector.

We compared the single bolometer, single survey maps with a model obtained with the following procedure:

- we pixelized the IRAM observations on a `HEALPix` grid with $N_{\text{side}} = 2048$, rotating to Galactic coordinates;
- we convolved these maps with the single bolometer, single survey effective beams using FEBeCoP (Mitra et al. 2011);
- using the Crab IRAM map as a template, and the polarization angles α, we modelled the intensity map described above in the Crab region as a function of an angular offset $\Delta\alpha$.

We then fitted for the values of the angular offset $\Delta\alpha$. To do that, we first removed the background from the single bolometer maps. We built a noise model combining the single detector pixel variance with the noise of the IRAM observation, taking into account the smoothing applied. We used the Rosset et al. (2010) values as a prior.

The resulting angular offsets are presented in Fig. 20. Corrections are compatible with zero, and this analysis does not favour an update of the ground-based parameters. We used the same procedure to fit the polarization efficiency ρ, but the result is completely dominated by the ground-based calibration prior.

If we assume that the CMB anisotropies have vanishing TB and EB power spectra, i.e. that there are no parity-violating
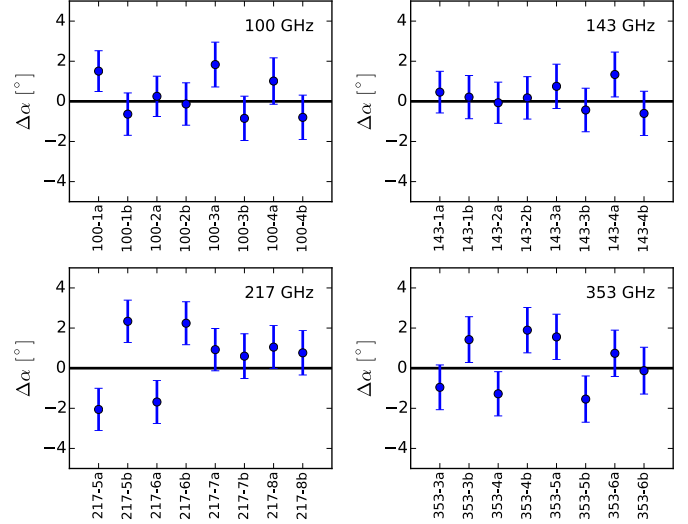

Fig. 20. Estimated angular offset from comparison of the single bolometer, single detector maps with the IRAM Crab nebula maps, combining the first four surveys.

physical mechanisms in the early Universe, we can also check whether the overall polarizer angle of *Planck*-HFI is compatible with zero. Planck Collaboration XXXI (in prep.) show that the CMB TB and EB spectra measured by HFI are consistent with zero. Their analysis gives a polarizer angle within 0.3° of zero, which is identical to the systematic error of the ground-based measurements. This is a factor of five improvement over the WMAP final results (Hinshaw et al. 2013) and is comparable with ACT (Naess et al. 2014; see also the review by Gubitosi & Paci 2013).

8. Conclusions

This paper has described the processing applied to construct the *Planck*-HFI maps delivered in the 2015 release. It has also assessed the main characteristics of the maps in terms of noise and systematics, in particular resulting from the analog-to-digital converter non-linearity correction and bolometer long time constants. Since the last release, the calibration has been upgraded and is now significantly more accurate. At low frequency, it is now independent and based on the orbital dipole signal, while the planets Uranus and Neptune are used to calibrate the high end of HFI, achieving 6.1 and 6.4% absolute photometric calibration at 545 and 857 GHz, respectively. This has allowed us to measure a consistent CMB solar dipole with an unprecedented accuracy better than 10^{-3} and in agreement with the independent determination by LFI.

Table 6 gives a quantitative assessment of the main characteristics of the *Planck* HFI maps from the 2015 release. They now cover the entire *Planck* HFI cold mission (885 days). The HFI aggregated sensitivity (referring to a weighted average of the 100, 143, and 217 GHz channel maps) is 26 μK$_{\text{CMB}}$ arcmin in temperature and 52 μK$_{\text{CMB}}$ arcmin in polarization.

The noise in the maps shows some small low-frequency excess in addition to white noise prior to time constant deconvolution. The latter then naturally raises the higher part of the noise spectra in the multipole domain. We have identified a low-level noise correlation in particular between half-ring and detector subsets that is not directly reproduced by simulations, although the level is low compared to the CMB signal.

Table 6. Main characteristics of HFI Full Mission Maps.

Quantity	100	143	217	353	545	857	Notes
Reference frequency ν [GHz]	100	143	217	353	545	857	[a1]
Number of bolometers	8	11	12	12	3	4	[a2]
Effective beam solid angle Ω [arcmin^2]	106.22	60.44	28.57	27.69	26.44	24.37	[b1]
Error in solid angle σ_Ω [arcmin^2]	0.14	0.04	0.04	0.02	0.02	0.02	[b2]
Spatial variation (rms) $\Delta\Omega$ [arcmin^2]	0.20	0.20	0.19	0.20	0.21	0.12	[b3]
Effective beam FWHM$_1$ [arcmin]	9.68	7.30	5.02	4.94	4.83	4.64	[b4]
Effective beam FWHM$_2$ [arcmin]	9.66	7.22	4.90	4.92	4.67	4.22	[b5]
Effective beam ellipticity ϵ	1.186	1.040	1.169	1.166	1.137	1.336	[b6]
Variation (rms) of the ellipticity $\Delta\epsilon$	0.024	0.009	0.029	0.039	0.061	0.125	[b7]
Sensitivity per beam solid angle [μK$_{CMB}$]	7.5	4.3	8.7	29.7			[c1]
[kJy sr^{-1}]					9.1	8.8	[c1]
Temperature sensitivity [μK$_{CMB}$ deg]	1.29	0.55	0.78	2.56			[c2]
[kJy sr^{-1} deg]					0.78	0.72	[c2]
Polarization sensitivity [μK$_{CMB}$ deg]	1.96	1.17	1.75	7.31			[c3]
Calibration accuracy [%]	0.09	0.07	0.16	0.78	1.1(+5)	1.4(+5)	[d]
CIB monopole [MJy sr^{-1}]	0.0030	0.0079	0.033	0.13	0.35	0.64	[e1]
Zodiacal light level correction [K$_{CMB}$]	4.3×10^{-7}	9.4×10^{-7}	3.8×10^{-6}	3.4×10^{-5}			[e2]
[MJy sr^{-1}]					0.04	0.12	[e2]

Notes. [a1] Channel map reference frequency and channel identifier. [a2] Number of bolometers whose data were used in producing the channel map. [b1] Mean value over bolometers at the same frequency. See Sect. 4.2 in Paper A. [b2] As given by simulations. [b3] Variation (rms) of the solid angle across the sky. [b4] FWHM of the Gaussian whose solid angle is equivalent to that of the effective beams. [b5] Mean FWHM of the elliptical Gaussian fit. [b6] Ratio of the major to minor axis of the best-fit Gaussian averaged over the full sky. [b7] Variability (rms) on the sky. [c1] Estimate of the noise per beam solid angle as given in [b1] . [c2] Estimate of the noise in intensity scaled to 1° assuming that the noise is white. [c3] Estimate of the noise in polarization scaled to 1° assuming that the noise is white. [d] Calibration accuracy (at 545 and 857 GHz: the 5% accounts for the model uncertainty). [e1] According to the Béthermin et al. (2012) model, whose uncertainty is estimated to be at the 20% level (also for constant νI_ν). [e2] Zero-level correction to be added on Zodical-light-corrected maps.

The raw sensitivity must be matched by a long list of constraints on any possible systematic effects. This list includes: an absolute calibration at a level from 0.1% to 1.4% depending on the frequency; a resulting apparent gain variation of less than 0.5%; and a knowledge of the polarization angle and polarization absolute value respectively at the degree level and the 1% level. The instrumental beam has been measured at the percent level by using multiple planet crossings.

Despite the huge progress made in the understanding of all the aforementioned systematic effects, *Planck*-HFI polarization maps are still dominated by systematic residuals at large scales. These are essentially coming from the temperature-to-polarization leakage resulting from the mismatch between the bolometers that are combined to reconstruct linear polarization maps. The origins of the leakage effects include mismatch of the zero level from uncertainty in the offset determination, mismatch from gain uncertainty (even at the 10^{-3} level), and bandpass mismatch. Corresponding first-order corrections for monopole, dipole, and bandpass mismatch are provided (as described in Appendix A.3.2), but residuals are still found to be larger than noise at very large scales. As a consequence, the *Planck*-HFI polarization maps at large scales cannot yet be directly used for cosmological studies.

References

Aumont, J., Conversi, L., Thum, C., et al. 2010, A&A, 514, A70
Béthermin, M., Daddi, E., Magdis, G., et al. 2012, ApJ, 757, L23
Fixsen, D. J. 2009, ApJ, 707, 916
Górski, K. M., Hivon, E., Banday, A. J., et al. 2005, ApJ, 622, 759
Gubitosi, G., & Paci, F. 2013, J. Cosmol. Astropart. Phys., 2, 20
Hinshaw, G., Weiland, J. L., Hill, R. S., et al. 2009, ApJS, 180, 225
Hinshaw, G., Larson, D., Komatsu, E., et al. 2013, ApJS, 208, 19
Kamionkowski, M., & Knox, L. 2003, Phys. Rev. D, 67, 063001
Kelsall, T., Weiland, J. L., Franz, B. A., et al. 1998, ApJ, 508, 44
Mather, J. C., Fixsen, D. J., Shafer, R. A., Mosier, C., & Wilkinson, D. T. 1999, ApJ, 512, 511
Mitra, S., Rocha, G., Górski, K. M., et al. 2011, ApJS, 193, 5
Moreno, R. 2010, Tech. Rep., ESA Herschel Science Center, ftp://ftp.sciops.esa.int/pub/hsc-calibration/PlanetaryModels/ESA2
Naess, S., Hasselfield, M., McMahon, J., et al. 2014, J. Cosmol. Astropart. Phys., 10, 7
Planck Collaboration VI. 2014, A&A, 571, A6
Planck Collaboration VIII. 2014, A&A, 571, A8
Planck Collaboration IX. 2014, A&A, 571, A9
Planck Collaboration XI. 2014, A&A, 571, A11
Planck Collaboration XIV. 2014, A&A, 571, A14
Planck Collaboration XXXI. 2014, A&A, 571, A31
Planck Collaboration I. 2016, A&A, 594, A1
Planck Collaboration II. 2016, A&A, 594, A2
Planck Collaboration III. 2016, A&A, 594, A3
Planck Collaboration IV. 2016, A&A, 594, A4
Planck Collaboration V. 2016, A&A, 594, A5
Planck Collaboration VI. 2016, A&A, 594, A6
Planck Collaboration VII. 2016, A&A, 594, A7
Planck Collaboration VIII. 2016, A&A, 594, A8
Planck Collaboration IX. 2016, A&A, 594, A9
Planck Collaboration X. 2016, A&A, 594, A10
Planck Collaboration XI. 2016, A&A, 594, A11
Planck Collaboration XII. 2016, A&A, 594, A12

Planck Collaboration XIII. 2016, A&A, 594, A13
Planck Collaboration XIV. 2016, A&A, 594, A14
Planck Collaboration XV. 2016, A&A, 594, A15
Planck Collaboration XVI. 2016, A&A, 594, A16
Planck Collaboration XVII. 2016, A&A, 594, A17
Planck Collaboration XVIII. 2016, A&A, 594, A18
Planck Collaboration XIX. 2016, A&A, 594, A19
Planck Collaboration XX. 2016, A&A, 594, A20
Planck Collaboration XXI. 2016, A&A, 594, A21
Planck Collaboration XXII. 2016, A&A, 594, A22
Planck Collaboration XXIII. 2016, A&A, 594, A23
Planck Collaboration XXIV. 2016, A&A, 594, A24
Planck Collaboration XXV. 2016, A&A, 594, A25
Planck Collaboration XXVI. 2016, A&A, 594, A26
Planck Collaboration XXVII. 2016, A&A, 594, A27
Planck Collaboration XXVIII. 2016, A&A, 594, A28
Planck HFI Core Team 2011, A&A, 536, A6
Quartin, M., & Notari, A. 2015, J. Cosmol. Astropart. Phys., 09, 050
Rosset, C., Tristram, M., Ponthieu, N., et al. 2010, A&A, 520, A13
Tauber, J. A., Norgaard-Nielsen, H. U., Ade, P. A. R., et al. 2010, A&A, 520, A2
Tristram, M., Filliard, C., Perdereau, O., et al. 2011, A&A, 534, A88

[1] APC, AstroParticule et Cosmologie, Université Paris Diderot, CNRS/IN2P3, CEA/lrfu, Observatoire de Paris, Sorbonne Paris Cité, 10 rue Alice Domon et Léonie Duquet, 75205 Paris Cedex 13, France

[2] African Institute for Mathematical Sciences, 6-8 Melrose Road, Muizenberg, 7945 Cape Town, South Africa

[3] Agenzia Spaziale Italiana Science Data Center, Via del Politecnico snc, 00133 Roma, Italy

[4] Aix Marseille Université, CNRS, LAM (Laboratoire d'Astrophysique de Marseille) UMR 7326, 13388 Marseille, France

[5] Astrophysics Group, Cavendish Laboratory, University of Cambridge, J J Thomson Avenue, Cambridge CB3 0HE, UK

[6] Astrophysics and Cosmology Research Unit, School of Mathematics, Statistics & Computer Science, University of KwaZulu-Natal, Westville Campus, Private Bag X54001, 4000 Durban, South Africa

[7] Atacama Large Millimeter/submillimeter Array, ALMA Santiago Central Offices, Alonso de Cordova 3107, Vitacura, 763 0355 Casilla, Santiago, Chile

[8] CITA, University of Toronto, 60 St. George St., Toronto, ON M5S 3H8, Canada

[9] CNRS, IRAP, 9 Av. colonel Roche, BP 44346, 31028 Toulouse Cedex 4, France

[10] CRANN, Trinity College, Dublin 2, Ireland

[11] California Institute of Technology, Pasadena, California CA 91125, USA

[12] Centre for Theoretical Cosmology, DAMTP, University of Cambridge, Wilberforce Road, Cambridge CB3 0WA, UK

[13] Computational Cosmology Center, Lawrence Berkeley National Laboratory, Berkeley, California, 92093-0424, USA

[14] DSM/Irfu/SPP, CEA-Saclay, 91191 Gif-sur-Yvette Cedex, France

[15] DTU Space, National Space Institute, Technical University of Denmark, Elektrovej 327, 2800 Kgs. Lyngby, Denmark

[16] Département de Physique Théorique, Université de Genève, 24, Quai E. Ansermet, 1211 Genève 4, Switzerland

[17] Departamento de Física, Universidad de Oviedo, Avda. Calvo Sotelo s/n, 33005 Oviedo, Spain

[18] Department of Astronomy and Astrophysics, University of Toronto, 50 Saint George Street, Toronto, Ontario ON M5S 3174, Canada

[19] Department of Astrophysics/IMAPP, Radboud University Nijmegen, PO Box 9010, 6500 GL Nijmegen, The Netherlands

[20] Department of Physics & Astronomy, University of British Columbia, 6224 Agricultural Road, Vancouver BC V6T 124, British Columbia, Canada

[21] Department of Physics and Astronomy, Dana and David Dornsife College of Letter, Arts and Sciences, University of Southern California, Los Angeles, CA 90089, USA

[22] Department of Physics and Astronomy, University College London, London WC1E 6BT, UK

[23] Department of Physics, Florida State University, Keen Physics Building, 77 Chieftan Way, Tallahassee, Florida, FL 32306, USA

[24] Department of Physics, Gustaf Hällströmin katu 2a, University of Helsinki, 00560 Helsinki, Finland

[25] Department of Physics, Princeton University, Princeton, New Jersey NJ 08540, USA

[26] Department of Physics, University of California, Santa Barbara, California CA 93106, USA

[27] Department of Physics, University of Illinois at Urbana-Champaign, 1110 West Green Street, Urbana, Illinois, IL 61801, USA

[28] Dipartimento di Fisica e Astronomia G. Galilei, Università degli Studi di Padova, via Marzolo 8, 35131 Padova, Italy

[29] Dipartimento di Fisica e Scienze della Terra, Università di Ferrara, via Saragat 1, 44122 Ferrara, Italy

[30] Dipartimento di Fisica, Università La Sapienza, P. le A. Moro 2, 00185 Roma, Italy

[31] Dipartimento di Fisica, Università degli Studi di Milano, via Celoria, 16, 20133 Milano, Italy

[32] Dipartimento di Matematica, Università di Roma Tor Vergata, via della Ricerca Scientifica, 1, 00133 Roma, Italy

[33] Discovery Center, Niels Bohr Institute, Blegdamsvej 17, 1165 Copenhagen, Denmark

[34] European Southern Observatory, ESO Vitacura, Alonso de Cordova 3107, Vitacura, Casilla 19001, Santiago, Chile

[35] European Space Agency, ESAC, Planck Science Office, Camino bajo del Castillo, s/n, Urbanización Villafranca del Castillo, Villanueva de la Cañada, Madrid, Spain

[36] European Space Agency, ESTEC, Keplerlaan 1, 2201 AZ Noordwijk, The Netherlands

[37] Facoltà di Ingegneria, Università degli Studi e-Campus, via Isimbardi 10, 22060 Novedrate (CO), Italy

[38] Gran Sasso Science Institute, INFN, viale F. Crispi 7, 67100 L'Aquila, Italy

[39] HGSFP and University of Heidelberg, Theoretical Physics Department, Philosophenweg 16, 69120 Heidelberg, Germany

[40] Helsinki Institute of Physics, Gustaf Hällströmin katu 2, University of Helsinki, 00100 Helsinki, Finland

[41] INAF–Osservatorio Astronomico di Padova, Vicolo dell'Osservatorio 5, 35141 Padova, Italy

[42] INAF–Osservatorio Astronomico di Roma, via di Frascati 33, 00078 Monte Porzio Catone, Italy

[43] INAF–Osservatorio Astronomico di Trieste, via G.B. Tiepolo 11, 34143 Trieste, Italy

[44] INAF/IASF Bologna, via Gobetti 101, 40127 Bologna, Italy

[45] INAF/IASF Milano, via E. Bassini 15, 28 Milano, Italy

[46] INFN, Sezione di Bologna, via Irnerio 46, 40126 Bologna, Italy

[47] INFN, Sezione di Roma 1, Università di Roma Sapienza, Piazzale Aldo Moro 2, 00185 Roma, Italy

[48] INFN, Sezione di Roma 2, Università di Roma Tor Vergata, via della Ricerca Scientifica, 1 Roma, Italy

[49] IPAG: Institut de Planétologie et d'Astrophysique de Grenoble, Université Grenoble Alpes, IPAG; CNRS, IPAG, 38000 Grenoble, France

[50] IUCAA, Post Bag 4, Ganeshkhind, Pune University Campus, 411 007 Pune, India

[51] Imperial College London, Astrophysics group, Blackett Laboratory, Prince Consort Road, London, SW7 2AZ, UK

[52] Infrared Processing and Analysis Center, California Institute of Technology, Pasadena, CA 91125, USA

[53] Institut Néel, CNRS, Université Joseph Fourier Grenoble I, 25 rue des Martyrs, 38054 Grenoble, France

[54] Institut Universitaire de France, 103 bd Saint-Michel, 75005 Paris, France

[55] Institut d'Astrophysique Spatiale, CNRS (UMR 8617) Université Paris-Sud 11, Bâtiment 121, 91405 Orsay, France

[56] Institut d'Astrophysique de Paris, CNRS (UMR 7095), 98 bis Boulevard Arago, 75014 Paris, France

[57] Institut für Theoretische Teilchenphysik und Kosmologie, RWTH Aachen University, 52056 Aachen, Germany

[58] Institute of Astronomy, University of Cambridge, Madingley Road, Cambridge CB3 0HA, UK

[59] Institute of Theoretical Astrophysics, University of Oslo, Blindern, 0371 Oslo, Norway

[60] Instituto de Física de Cantabria (CSIC-Universidad de Cantabria), Avda. de los Castros s/n, Santander, Spain

[61] Istituto Nazionale di Fisica Nucleare, Sezione di Padova, via Marzolo 8, 35131 Padova, Italy

[62] Jet Propulsion Laboratory, California Institute of Technology, 4800 Oak Grove Drive, Pasadena, California, CA 91109, USA

[63] Jodrell Bank Centre for Astrophysics, Alan Turing Building, School of Physics and Astronomy, The University of Manchester, Oxford Road, Manchester, M13 9PL, UK

[64] Kavli Institute for Cosmological Physics, University of Chicago, Chicago, IL 60637, USA

[65] Kavli Institute for Cosmology Cambridge, Madingley Road, Cambridge, CB3 0HA, UK

[66] Kazan Federal University, 18 Kremlyovskaya St., 420008 Kazan, Russia

[67] LAL, Université Paris-Sud, CNRS/IN2P3, Orsay, France

[68] LERMA, CNRS, Observatoire de Paris, 61 Avenue de l'Observatoire, 75014 Paris, France

[69] LESIA, Observatoire de Paris, CNRS, UPMC, Université Paris-Diderot, 5 Place J. Janssen, 92195 Meudon, France

[70] Laboratoire AIM, IRFU/Service d'Astrophysique – CEA/DSM – CNRS – Université Paris Diderot, Bât. 709, CEA-Saclay, 91191 Gif-sur-Yvette Cedex, France

[71] Laboratoire Traitement et Communication de l'Information, CNRS (UMR 5141) and Télécom ParisTech, 46 rue Barrault, 75634 Paris Cedex 13, France

[72] Laboratoire de Physique Subatomique et Cosmologie, Université Grenoble-Alpes, CNRS/IN2P3, 53 rue des Martyrs, 38026 Grenoble Cedex, France

[73] Laboratoire de Physique Théorique, Université Paris-Sud 11 & CNRS, Bâtiment 210, 91405 Orsay, France

[74] Lawrence Berkeley National Laboratory, Berkeley, California, CA 94720, USA

[75] Lebedev Physical Institute of the Russian Academy of Sciences, Astro Space Centre, 84/32 Profsoyuznaya st., GSP-7, 117997 Moscow, Russia

[76] Max-Planck-Institut für Astrophysik, Karl-Schwarzschild-Str. 1, 85741 Garching, Germany

[77] McGill Physics, Ernest Rutherford Physics Building, McGill University, 3600 rue University, Montréal, QC, H3A 2T8, Canada

[78] National University of Ireland, Department of Experimental Physics, Maynooth, Co. Kildare, Ireland

[79] Nicolaus Copernicus Astronomical Center, Bartycka 18, 00-716 Warsaw, Poland

[80] Niels Bohr Institute, Blegdamsvej 17, 2100 Copenhagen, Denmark

[81] Optical Science Laboratory, University College London, Gower Street, London WC1E 6BT, UK

[82] SISSA, Astrophysics Sector, via Bonomea 265, 34136 Trieste, Italy

[83] School of Physics and Astronomy, Cardiff University, Queens Buildings, The Parade, Cardiff, CF24 3AA, UK

[84] School of Physics and Astronomy, University of Nottingham, Nottingham NG7 2RD, UK

[85] Sorbonne Université-UPMC, UMR 7095, Institut d'Astrophysique de Paris, 98 bis Boulevard Arago, 75014 Paris, France

[86] Space Sciences Laboratory, University of California, Berkeley, California CA 94720, USA

[87] Special Astrophysical Observatory, Russian Academy of Sciences, Nizhnij Arkhyz, Zelenchukskiy region, 369167 Karachai-Cherkessian Republic, Russia

[88] Sub-Department of Astrophysics, University of Oxford, Keble Road, Oxford OX1 3RH, UK

[89] Theory Division, PH-TH, CERN, 1211 Geneva 23, Switzerland

[90] UPMC Univ Paris 06, UMR 7095, 98 bis Boulevard Arago, 75014 Paris, France

[91] Université de Toulouse, UPS-OMP, IRAP, 31028 Toulouse Cedex 4, France

[92] University of Granada, Departamento de Física Teórica y del Cosmos, Facultad de Ciencias, 18001 Granada, Spain

[93] University of Granada, Instituto Carlos I de Física Teórica y Computacional, 18003 Granada, Spain

[94] Warsaw University Observatory, Aleje Ujazdowskie 4, 00-478 Warszawa, Poland

Appendix A: HFI map product description

Here we summarize the HFI map products that are part of the Planck 2015 data release.

A.1. Map products

The 2015 release contains many different maps whose details are described below. All maps are given as `HEALPix` vectors with NESTED ordering in Galactic coordinates at the resolution corresponding to N_{side} = 2048 (for high resolution maps). Depending on the type of product, these vectors are packaged into a binary table and written into a FITS file. The table contains in most cases 50 331 648 rows (the length of the `HEALPix` vector for N_{side} = 2048) and either three columns (I, II, H for intensity, noise (co)variance, and hits, respectively) for the temperature-only cases or ten columns (I, Q, and U signals plus the six various I, Q, and U noise (co)variances and hits) for the polarized cases. Pixels with a condition number larger than 10^3 see their hit number brought down to zero. A pixel with zero hits has an intensity value of -1.6375×10^{30} (the `HEALPix` conventional null value).

The general matrix of products is pictured in Fig. 4. The main products are the maps of the full channels covering the full mission. For characterization and analysis purposes, the channels have been split into independent detector sets. The detector sets for the polarized channels are groups of four polarization-sensitive bolometers that can be used to build a sky map in temperature and polarization. Bolometers insensitive to polarization (Spider-Web Bolometers) of the same frequency channels are not used in the detector sets. The detector set names and the bolometers they use are listed in Table A.1. For completeness, full mission maps built using each of the unpolarized bolometers are also provided.

The mission duration has been split into single surveys, years, and the two halves of the mission duration. The surveys are defined as the observations within a contiguous rotation range of 180° for the spin axis, and as a consequence each survey does not cover the full sky. We note that the fifth survey had not been completed when HFI stopped observing, and was also interrupted by various end-of-mission tests. That last survey was also performed with a different scanning strategy than the first four surveys (Planck Collaboration I 2016). The date and ring number corresponding to the beginning and end of each time split are summarized in Table A.2. Single survey maps are provided for the full channels only. Yearly maps are provided for Year 1 and Year 2 for the full channels, the detector sets and each of the Spider-Web Bolometers, where the years span Surveys 1–2 and 3–4. Half-mission maps are also provided, where each half contains one half of the valid rings (or stable pointing periods). There are 347 discarded rings (and 26 419 valid ones), most of which occurred during the partial last survey when various end-of-life tests were performed.

Half-ring maps are produced by splitting each ring into two parts of equal duration. The difference of the two half-ring maps provides a useful estimate of the high-frequency noise and possibly of other systematics. We note that this is the only case where the destriping offsets are different from the offsets in the standard case. Half-ring maps are provided for the full mission only. They are given for the full channels, the detector sets, and the Spider-Web Bolometer maps.

Maps are corrected for zodiacal light emission. Correction maps are also provided for the frequency maps and the various time splits.

Units are K_{CMB} for frequencies up to 353 GHz and MJy sr^{-1} assuming a constant νI_ν law above.

A.2. Stokes parameter correlations

The *Planck* HFI delivery includes pixelized maps of Stokes covariances (II, IQ, IU, QQ, QU, UU) solved during the map-making process for each pixel independently.

In Fig. A.1 we present the distribution of the I, Q, and U correlations in each pixel for the HFI frequencies where polarization is reconstructed.

A.3. Leakage correction maps

Section 7.3 describes the origin and the formalism of the intensity-to-polarization leakage in HFI and how it is, in principle, possible to quantify and correct for these systematic effects. This is particularly important for any studies of the large angular scales in polarization where dipole, monopole, and dust leakages are the main limiting factors.

Although dust and CO bandpass leakage effects can be estimated from given intensity templates and electromagnetic spectra (Sect. A.3.1), this is not the case for the calibration and monopole leakage levels, which have to be estimated directly from the maps (Sect. A.3.2).

A.3.1. Bandpass leakage correction maps

The small differences in the bandpasses of the different bolometers combined to produce polarization maps give rise to some leakage from intensity to polarization for the CO and the (Galactic) dust emission; this is estimated using the known band profiles and templates of the emission (see Sect. 7.3.1).

Bandpass leakage Q and U maps are provided for dust for all channels, using ground-based measurement of the bandpass integrated over the dust emission law. Each FITS file contains a single extension, with two columns containing the Q and U leakage maps in K_{CMB} units.

A.3.2. The generalized global fit (GGF) approach for leakage correction

The generalized global fit (GGF) method is a template fitting approach that has been developed to consistently solve for calibration, monopole, and bandpass mismatch leakage effects at the map level. Each Q and U map at 100, 143, 217, and 353 GHz is modelled as

$$[Q, U]^\nu = [Q, U]_{CMB} + [Q, U]^\nu_{dust} \qquad (A.1)$$
$$+ \sum_{b\in\nu} \alpha^\nu_b \Gamma^b_{IQ,IU} + \sum_{b\in\nu} \beta^\nu_b \Gamma^b_{IQ,IU} \times I^{dipole}$$
$$+ \sum_{b\in\nu} \gamma^\nu_b \Gamma^b_{IQ,IU} \times I^{dust} + \sum_{b\in\nu} \delta^\nu_b \Gamma^b_{IQ,IU} \times I^{CO} ,$$

where

- the first line corresponds to the physical polarization signal coming from the CMB and the dust (synchrotron is assumed negligible at these frequencies);
- the second line corresponds to the monopole and calibration leakage terms, the templates of which make use of the leakage pattern maps Γ described in Sect. 7.3;

Table A.1. Detector set definitions.

Frequency	DetSet1	DetSet2
100 GHz	100-1a/b 100-4a/b	100-2a/b 100-3a/b
143 GHz	143-1a/b 143-3a/b	143-2a/b 143-4a/b
217 GHz	217-5a/b 217-7a/b	217-6a/b 217-8a/b
353 GHz	353-3a/b 353-5a/b	353-4a/b 353-6a/b
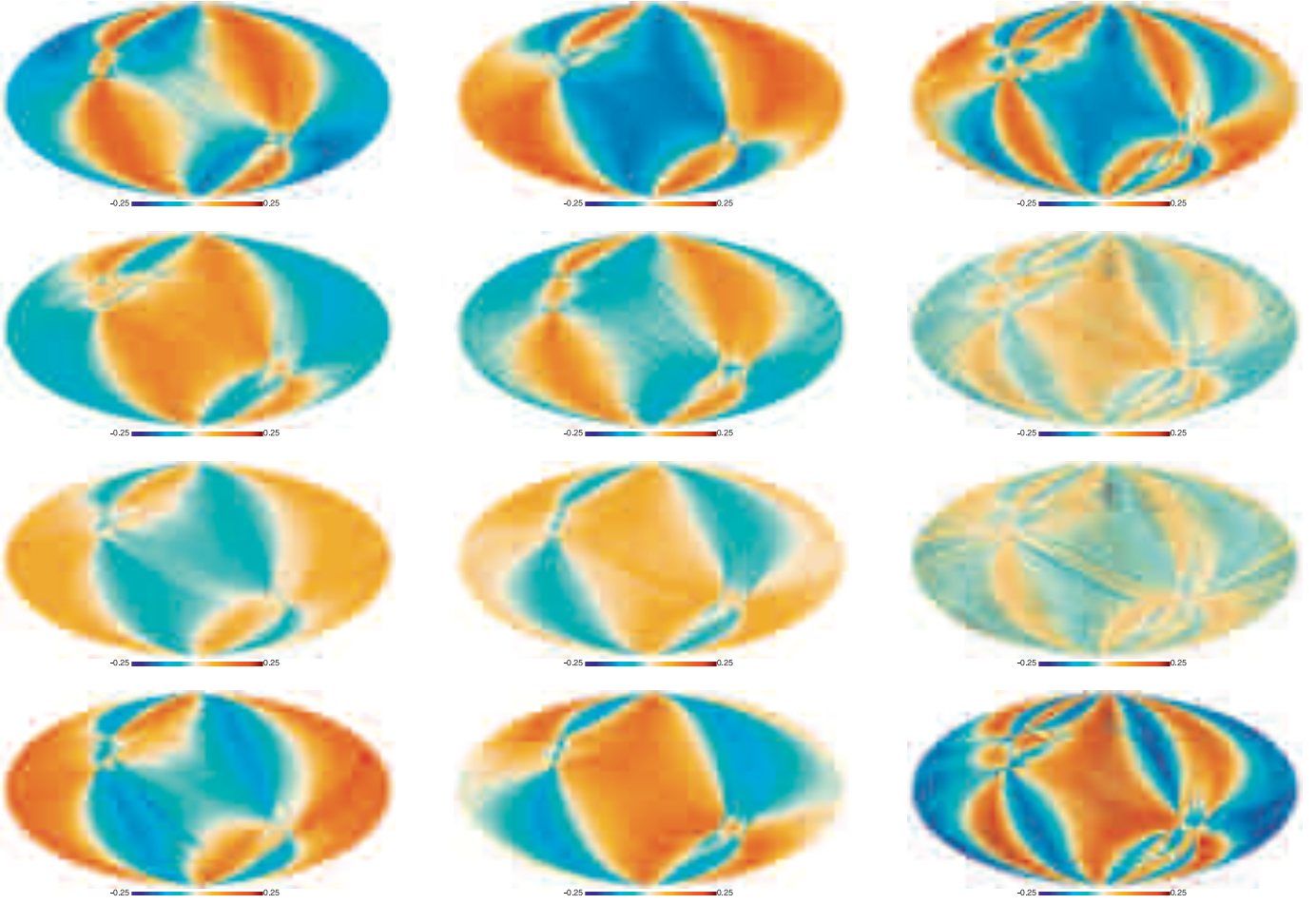
Fig. A.1. Maps of the correlation *IQ* (*left*), *IU* (*middle*), and *QU* (*right*) between Stokes parameters for the 100, 143, 217, and 353 GHz (*from top to bottom*).

Table A.2. Date and ring numbers for the beginning and end of each time split.

Time split	Start date	First ring	End date	End ring
Full mission	2009-Aug.-12	240	2012-Jan.-13	27 005
Nominal mission	2009-Aug.-12	240	2010-Nov.-28	14 723
Half mission 1	2009-Aug.-12	240	2010-Oct.-15	13 471
Half mission 2	2010-Oct.-15	13 472	2012-Jan.-13	27 005
Year 1	2009-Aug.-12	240	2010-Aug.-12	11 194
Year 2	2010-Aug.-12	11 195	2011-Jul.-29	21 720
Survey 1	2009-Aug.-12	240	2010-Feb.-08	5720
Survey 2	2010-Feb.-08	5721	2010-Aug.-12	11 194
Survey 3	2010-Aug.-12	11 195	2011-Feb.-08	16 691
Survey 4	2011-Feb.-08	16 692	2011-Jul.-29	21 720
Survey 5	2011-Jul.-29	21 721	2012-Jan.-13	27 005

- the dust and CO bandpass-missmatch leakage terms are gathered in the third line, again using the leakage patterns maps Γ;
- each summation is performed over the polarized bolometers of the frequency channel ν.

We use the *Planck* 353 GHz Q and U maps as polarized dust templates and perform the fitting procedure at $1°$ resolution and $N_{\mathrm{side}} = 64$. Focusing on polarized dust and leakage effects only, Eq. (A.1) becomes

$$[Q, U]^{\nu} = (1 - \epsilon^{\nu})\,[Q, U]_{\mathrm{CMB}} + \epsilon^{\nu}\,[Q, U]^{353} \qquad (A.2)$$
$$+ \sum_{b \in \nu} \alpha_b^{\nu} \Gamma_{IQ,IU}^b + \sum_{b \in \nu} \beta_b^{\nu} \Gamma_{IQ,IU}^b \times I^{\mathrm{dipole}}$$
$$+ \sum_{b \in \nu} \gamma_b^{\nu} \Gamma_{IQ,IU}^b \times I^{\mathrm{dust}} + \sum_{b \in \nu} \delta_b^{\nu} \Gamma_{IQ,IU}^b \times I^{\mathrm{CO}}$$
$$- \epsilon^{\nu} \times \left[\sum_{b \in 353} \alpha_b^{353} \Gamma_{IQ,IU}^b + \sum_{b \in 353} \beta_b^{353} \Gamma_{IQ,IU}^b \times I^{\mathrm{dipole}} \right.$$
$$\left. + \sum_{b \in 353} \gamma_b^{353} \Gamma_{IQ,IU}^b \times I^{\mathrm{dust}} + \sum_{b \in 353} \delta_b^{353} \Gamma_{IQ,IU}^b \times I^{\mathrm{CO}} \right],$$

where ϵ^{ν} is the overall factor scaling the dust from 353 GHz to the frequency channel ν and where α, β, γ, and δ define the amplitude of the monopole, dipole, dust, and CO leakage effects, respectively. The last two lines of Eq. (A.2) correct for the total leakage added when using $[Q, U]^{353}$ as dust templates. This equation is at the core of the GGF method, which is then implemented as follows:

1. A first fit is performed to solve for the coefficients of Eq. (A.2), for each channel ($\nu = 100$, 143, and 217 GHz) independently. There are strong degeneracies between the leakage templates at frequency ν and at 353 GHz, so that this first fit does not provide reliable α, β, γ, and δ coefficients that can be used to compute leakage correction maps. However, it enables an accurate determination of the overall scaling factor of the dust ϵ^{ν} between the channel under scrutiny and 353 GHz.
2. These ϵ^{ν} values are used as inputs to solve Eq. (A.2), simultaneously for all channels, in a consistent manner. At this stage, we add some extra constraints (such as minimizing detector-set and survey differences) in order to reduce the leakage degeneracies between the four channels. This generalized global fit allows us to extract the set of α, β, γ, and δ for all HFI polarized channels, including 353 GHz.
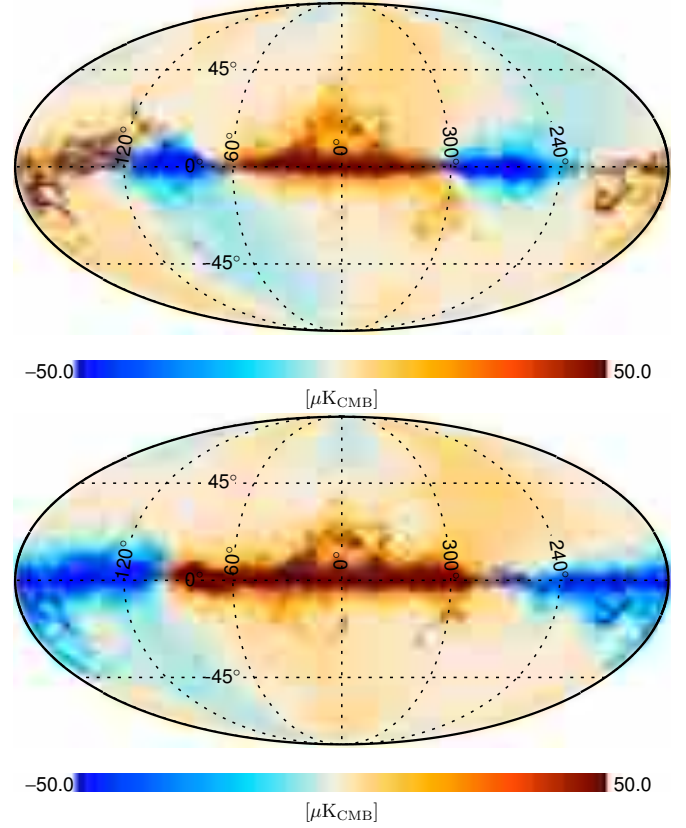

Fig. A.2. Total leakage correction maps in Q (*top*) and U (*bottom*) at 353 GHz computed with the generalized global fit (GGF) method, which includes leakages from calibration, CO, and dust.

Solving for survey differences in the second step is crucial. Although the leakage coefficients are independent of scan angle, the Γ maps change because pixels are scanned at different angles in different surveys. Total leakage maps, allowing a correction for leakages induced by monopole, calibration, and bandpass mismatches, are then computed using the coefficients extracted in the second step of the procedure. Figure A.2 shows the total correction in Q (top) and U (bottom) for the 353 GHz channel. Dust and CO bandpass-mismatch leakage effects are clearly dominant near the Galactic plane, while the large patterns at high latitude are mainly due to the dipole leakage.